UNMIXING ALGORITHMS AND MATERIALS FOR RADIATION DETECTION IN HARSH ENVIRONMENTS

BY

MATTHEW A. WEISS

THESIS

Submitted in partial fulfillment of the requirements
for the degree of Master of Science in Nuclear, Plasma, and Radiological Engineering
in the Graduate College of the
University of Illinois at Urbana-Champaign, 2022

Urbana, Illinois

Master's Committee:

Assistant Professor Angela Di Fulvio, Advisor
Professor Mohan Sankaran

Abstract

Spectroscopy-grade radiation measurements need to be performed in harsh environments for several applications, such as radiological search, decommissioning, and remediation. In harsh environments, there may be many shielded and bare radionuclides present simultaneously, the detector may be damaged by the radiation, and other environmental effects may degrade its performance. This work focuses on tackling these issues from both a hardware and software perspective, including the development of unmixing algorithms for source identification, and a methodology for growing diamond as a radiation-hardened material for powering remote sensors and for radiation detection.

Source identification is particularly challenging when using organic scintillators. These detectors can be grown in large sizes and are sensitive to both gamma-rays and neutrons, through pulse shape discrimination, but their energy resolution is limited. Hence discriminating different sources directly from their spectral differences is a challenging task. To solve this issue, we first demonstrated that Bayesian unmixing algorithms applied to organic scintillator spectra can reliably identify unshielded gamma-ray radionuclides, even with fewer than 1,000 detected counts and in the presence of two or three nuclides at the same time. We experimentally studied the robustness of a state-of-the-art unmixing algorithm to different radiation background spectra, due to varying atmospheric conditions, in the 16 °C to 28 °C temperature range. In the presence of background, the algorithm is able to identify the nuclides present in unknown radionuclide mixtures of three nuclides, when at least 1,000 counts from the sources are detected. With fewer counts available, we found larger differences of approximately 35.9% between estimated nuclide fractions and actual ones. In these low count rate regimes, the uncertainty associated with the result that is provided by our algorithm with the identified fractions could be an additional valuable tool to determine whether the identification is reliable or a longer measurement to increase the

signal-to-noise ratio is needed.

We then applied the unmixing algorithm to identify shielding materials in the detection of a shielded source. A series of experiments was performed at the Device Assembly Facility at the Nevada National Security Site to test the usage of a deuterated trans-stilbene organic scintillation (stilbene-d_{12}) detector on a shielded 4.5 kg sphere of alpha-phase plutonium surrounded by stainless steel cladding and shielded by various materials, including polyethylene and lead. These measurements required a series of post-processing steps, including calibration, pile-up rejection (PUR), and pulse-shape discrimination (PSD). Optimizing the PUR parameters allowed for a neutron detection efficiency of 34.4±0.2% with a neutron rejection fraction of 8.02 %. Once processed, these neutron spectra were used to validate a simulated model of the shielded SNM detection. I simulated the stilbene-d_{12} light output response matrix in the 0.1 to 20 MeV range based on the stilbene-d_{12} light output response measured at the Nuclear Measurement Lab. Four unmixing testing scenarios were employed to test the feasibility of using the unmixing algorithm for identifying shielding materials. The algorithm is able to identify the simulated shielding components in a mixed shielded spectra scenario when at least 50,000 counts are detected from the source. Lastly, the algorithm is able to correctly identify shielded light output spectra and unfolded neutron energy spectra with a 99.9% certainty with the addition of Poisson noise.

The second part of this thesis details the preliminary construction and development of a plasma reactor to grow diamond using the chemical vapor deposition (CVD) method. The reactor design allows for a diamond film to be formed on the surface of a substrate for various uses such as in diamond-based betavoltaic cells and diamond detector materials. Diamond is an attractive material for application in harsh environments due to its radiation hardness and large indirect band-gap of 5.5 eV. The proposed reactor design was simulated in COMSOL for verifying adequate heat dissipation from the high temperature substrate heating needed for diamond layer creation. This simulation confirms the ability for the chamber to maintain a temperature increase of 120–140 °C, while the maximum temperature never exceeds 300 °C. Lastly, the reactor was constructed for upcoming plasma-enhanced diamond CVD with a remote radio-frequency (RF) plasma.

Acknowledgments

I would like to thank my family and friends for supporting me throughout my college and graduate school years. I could not have done it without everyone's love, kindness, and encouragement. Thank you especially to my Mom, Dominick, Evan, and Effie for their unwavering love and guidance throughout my life.

I would like to additionally thank my advisor, Professor Angela Di Fulvio, for all of her support and guidance over the past 2+ years. I have significantly grown and developed as a researcher since I started in the NML as an undergraduate researcher, and I owe much of my success to your direction. Additionally, I would like to thank Professor Mohan Sankaran for his assistance and patience in helping me navigate a new direction for my research. Thank you both for your reviews and revisions on this thesis and being a part of my master's committee.

The National Criticality Experiments Research Center (NCERC) work is supported by the DOE Nuclear Criticality Safety Program, funded and managed by the National Nuclear Security Administration for the Department of Energy. I would also like to thank the Los Alamos National Laboratory (LANL) and Mission Support and Test Services (MSTS) for their role in executing these experiments.

This material is based upon work supported under a Department of Energy Nuclear Energy University Programs Graduate Fellowship.

Table of Contents

List of Abbreviations

BeRP	Beryllium-Reflected Plutonium
BTG	Bernoulli-truncated Gaussian
CVD	Chemical Vapor Deposition
DAF	Device Assembly Facility
D-T	Deuterium-Tritium
eVee	Electron-volt Electron Equivalent
LET	Linear Energy Transfer
LO	Light Output
MCMC	Markov-Chain Monte Carlo
MFC	Mass Flow Controller
MPH	Minimum Peak Height
MPR	Minimum Peak Ratio
NCERC	National Criticality Experiments Research Center
NRF	Neutron Rejection Fraction
PE	Polyethylene
PSD	Pulse-shape Discrimination
PUR	Pile-up Rejection
RF	Radio Frequency
SNM	Special Nuclear Material
stilbene-d_{12}	Deuterated Trans-stilbene
TTR	Tail-to-Total Ratio

Chapter 1

Introduction

Spectroscopy-grade radiation measurements need to be performed in harsh environments for several applications, such as radiological search, decommissioning, and remediation [1]. In harsh environments, there may be many shielded and bare radionuclides present simultaneously, the detector may be damaged by the radiation, and other environmental effects may degrade the energy resolution of the detectors. Energy resolution is a parameter of merit that determines the minimum difference in emitted energy that a detector is able to resolve and it should be minimized to improve nuclide identification and imaging contrast. This work focuses on tackling these issues from both a hardware and software perspective, including the development of unmixing algorithms for source identification, and a methodology for growing diamond as a radiation-hardened material for powering remote sensors and for radiation detection. In harsh environments and remote locations, detecting the presence of special nuclear material (SNM) is a challenging task. SNM includes plutonium, uranium-233, or uranium enriched in the isotopes uranium-233 or uranium-235. These isotopes produce prompt fission neutrons whose energy spectral distribution can be described by a characteristic Watt fission spectrum. A variety of shielding materials may be used to mask the SNM's radiation signature for illicit purposes, such as overt or covert nuclear proliferation efforts [2, 3]. For example, a plutonium source may be shielded by lead and polyethylene to help reduce dosage and modulate the detected spectrum to obstruct its identification. In cases such as these, finding the identity of the SNM source becomes more difficult as many of the main features of the detected spectra are significantly attenuated. However, the signatures can still be identified if the shielding material and its thickness can be determined since the shielding effect on the neutron spectrum is directly related to the material type and neutron cross section. In this case, an unmixing algorithm can be suitably used to identify the materials used

for shielding and/or the source spectrum.

In this thesis, I demonstrate the use of an unmixing algorithm that uses a library of neutron spectra modulated by different materials to compare a measured spectrum against. Using Bayesian statistical methods, the algorithm can identify the components of the shielding mixture. We have shown that this methodology is effective at identifying gamma signatures using a library of gamma-decay radioisotopes measured using a EJ-276 organic scintillation detector [4]. Building upon that work, we adjusted the algorithm to take a library of SNM neutron spectra shielded by different materials that have been detected by a deuterated trans-stilbene (stilbene-d_{12}) organic scintillation detector as input. Measured fast-neutron spectra are a weak function of the interacting neutron energy and are smoothly modulated by the shielding materials, therefore neutron spectroscopy and shielding-material identification is a challenging task. Additionally, the thickness of the shielding material also changes the degree to which the radiation signature will be changed. Implementing these changes into the unmixing algorithm allows for it to become robust in many situations, while remaining a fast method for verification. Neutron-induced gamma-ray signatures could be used for shielding material identification. However, owing to their higher penetrability, I focused my work on fast neutron detection.

The second portion of my work focuses on material development for use in harsh environments. With radiation damage largely impacting the performance of a detector and degrading the material, new detection materials that can withstand higher fluence are needed to improve usability in these regions. Being inherently radiation-resistant, diamond is an attractive material for use in high-radiation fields for several applications, ranging from durable power supply, when used in betavoltaic mode [5, 6, 7], to radiation detection [8, 9, 10]. The main goals for this research were to create a deposition chamber for depositing a thin layer of diamond on a silicon wafer using methane gas. This chamber makes use of plasma-enhanced chemical vapor deposition (CVD), where a plasma makes contact with the substrate surface and slowly deposits a thin layer of diamond, when the chamber is operated at the proper temperature and pressure. The procedure for creating this assembly is detailed further in Chapter 3, including further theory behind how CVD is performed and what parameters are used to deposit diamond.

1.1 Shielded Radioisotope Identification

In a treaty verification scenario, the correct identification of shielded isotopes is a vital step in making sure that unknown sources match the composition that is being declared. Many of the challenges that are faced are dependent on the shielding material altering the spectra that the isotope gives off. Regardless of the purpose of the shielding materials, trying to identify the underlying SNM source adds an additional layer of complexity to understand its composition. One possible solution to this problem is being able to back-calculate the spectra of the source based on the knowledge of how different shielding materials alter neutron source spectra. This objective can be accomplished in a number of ways, with the unmixing of the source spectra into its components being the main investigation of this thesis. If the unmixing algorithm can reliably output the correct shielding component and the presence of an SNM source, then this methodology can be used in many different security applications, including search, imaging, and warhead verification.

Taking the shielding data from SNM was performed at the Device Assembly Facility (DAF) in the Nevada National Security Site. The DAF facility provided the opportunity to take measurement data from a 4.5 kg sphere of alpha-phase plutonium surrounded by stainless steel cladding, called the BeRP ball [11]. At the DAF, an experimental set up was created and I took measurements of this BeRP ball in four different shielded configurations: shielded by 2-inches of polyethylene (PE), 2-inches of lead, 1-inch of each PE and lead, and an *Unshielded* (bare source) configuration. The detector that was used is a organic scintillation detector, which is a detector that the Nuclear Measurement group has contributed to developing and characterizing and exhibits excellent pulse shape discrimination and neutron spectroscopy abilities due to the presence of the deuteron in the stilbene matrix [12] [13]. As such, the decay products of the alpha-phase plutonium, including americium-241, can have their gamma-decay spectra more accurately separated from the spectra of the desired neutrons.

The process of separating these spectra utilizes pulse-shape discrimination (PSD) methods, which are described in more detail in Section 2.3. Pulse-shape discrimination allows for the neutron pulses to be accurately separated from the gamma-ray pulses during the post processing steps using a pulse shape parameter. Using this method, we can separate out the neutron pulses

and derive the pulse integral distribution, i.e., the light-output spectrum. The light-output spectrum shows the distribution of the energy deposited within the detector, suitably modulated by the material scintillation quenching functions [14]. An unfolding algorithm was used to find the neutron energy spectrum that is incident on the detector, given the measured light output spectrum and the simulated detector response to monoenergetic neutrons. This neutron energy spectra have been modified as a result of the shielding material's ability to interact with particles differently at different energies. This modulating effect can be characterized by the material's cross section. Calculating how the BeRP ball's energy spectra is modified as a result of the material cross-section provided an accurate estimate for what the shielded neutron energy spectra. These unfolded spectra were then used to test the ability of the unmixing algorithm to predict the type of shielding material. The unmixing algorithm has been shown to be effective in gamma radioisotope applications [4], and this project aims to extend the algorithm's applications to shielded SNM sources. Details on how the unfolding and unmixing processes are performed can be found in Chapter 2.

1.2 Plasma-Enhanced Chemical Vapor Deposition of Diamond

Performing CVD for diamond growth is done through the chemical reaction of flowing precursor gases with a heated substrate surface, resulting in the deposition of a thin diamond film on the substrate. The diamond lattice is constructed layer-by-layer through the adsorption of hydrogen on the surface creating an open site for CH_3 radicals to be deposited [15]. Once these radicals are deposited and additional hydrogen atoms are removed, two adjacent carbon atoms may bond to add to the diamond lattice. As more carbon atoms are added onto the lattice, a thin film of diamond starts to form with a growth rate that is determined by many factors in this process, such as methane partial-pressure, temperature of substrate, gas flow rates, and plasma to substrate distance [16]. Additionally, the ratio of methane to hydrogen inputs needs to be approximately 1%:99% to grow many thin layers of diamond using a plasma-enhanced CVD chamber, as a large amount of hydrogen is needed to maintain a fast adsorption speed [17]. If there is

too much methane being inserted, there is a greater chance for defects that cause graphite to form rather than a diamond lattice. Once the deposition is complete, the film can be analyzed with a scanning electron microscope and using micro Raman spectroscopy to check for any possible defects. These defects can cause diminishing efficiency in the detection material application as the transport of charge is most effective in the uniform diamond structure, making reducing these defects a necessity for producing films with minimum defect density.

The process of creating the diamond layer uses a reactor chamber setup that was designed and simulated for use in the deposition of diamond. The chamber design uses a small cubic chamber that can be outfitted with flanges on all sides for various purposes. One end constitutes the input, where a plasma enters the chamber while being created by a signal-matched radio-frequency (RF) plasma consisting of a methane and hydrogen mixture. Another end constitutes a vacuum output, where a vacuum pump is used to lower the pressure inside of the chamber to maintain the plasma structure. Lastly, one side will be used to measure pressure using a convectron pressure sensor, and another will contain the substrate heater and holder. When in use, the substrate heater will keep the substrate at about 900°C in order to get proper diamond deposition. This procedure allows for the vapor deposition to take place on the substrate surface as proper temperature and pressure conditions must be met for the diamond lattice to be built upon. Additionally, a COMSOL model was built and tested over the deposition timeline to confirm that the chamber would be able to withstand these temperature and pressure conditions.

Chapter 2

Shielded SNM Identification

2.1 Introduction and Motivation

Detecting shielded neutron sources is a challenging task relevant to radiological search and nuclear security. For example, at radiation portal monitors installed at most national ports and airports, it can be difficult to perform nuclide detection above background and identification using only a passive measurement of gamma rays. With a short acquisition time window for these measurements, identification of a radiation source must be done with a relatively small amount of data. The shielding effect compounds this issue, with each shielding material modulating the emitted spectrum. The methodology reported in this thesis tests the effect of shielding materials on the spectrum of a special nuclear material (SNM) fission source. Then a spectral unmixing algorithm is applied to identify the shielding material. The suitability of using the spectroscopy-capable organic scintillator stilbene-d_{12} is also evaluated. In this work, I studied the unmixing algorithm's performance at unmixing spectra from shielded neutron sources to retrieve the shielding material. The identification of these spectra poses a particular challenge because their shape from each shielding setup tends to be very similar in the energy range to which the detector is sensitive, i.e., 500 keV to 20 MeV neutron energy. Additionally, I report on the experimental validation of a simulated detection setup measuring shielded configurations of the BeRP ball, a 4.48 kg α-phase plutonium sphere, and I tested the identification performance of the unmixing algorithm on experimentally-validated simulated light output data. This data was then used in comparison with a proposed unmixing methodology using a library of cross-section modified BeRP ball spectra. The application of this methodology would allow for more diverse shielding material libraries to be created simply using a bare SNM source spectra and the cross section data for the shielding material. This chapter further explores this methodol-

ogy by showing the spectra modifications performed, demonstrating neutron spectra unfolding from light output data, and finally testing the algorithm's effectiveness in identifying unknown shielded neutron spectra.

2.2 DAF Data Acquisition

In order to perform shielded measurements on special nuclear materials, the experiments were performed at the Device Assembly Facility (DAF) in the National Criticality Experiments Research Center (NCERC). This set of experiments were performed using a stilbene-d_{12} organic scintillation detector (stilbene-d_{12}) [18, 19, 13] and a set of shielding materials placed in between the SNM source and the detector. The source being used is the BeRP ball, which is a 4.48-kg sphere of α-phase plutonium, surrounded by a 0.3 mm layer of SS304 stainless steel cladding [20]. The BeRP ball diameter is 7.717 cm, including the surrounding cladding material. Each experiment tested a different configuration of shielding materials and thicknesses between the detector and the BeRP ball. The types of shielding material used were lead and polyethylene slabs, with the polyethylene (PE) being separated into 2.54-cm-thick slabs and each lead slab being 6.35-mm-thick. Four different combinations of shielding layers were used: (a) unshielded, (b) 5.08-cm-thick lead layer, (c) 5.08-cm-thick PE layer, and (d) 2.54-cm-thick PE layer followed by 2.54-cm-thick lead layer. The detector was a 140 cm^3 volume stilbene-d_{12} crystal, grown at Lawrence Livermore National Laboratory[19] of non-equilateral hexagonal prismatic shape (Fig. 2.1.a).

As shown in Fig. 2.1.b, the distance between the BeRP center and detector front face was 1 meter to reduce the total fluence rate impinging on the detector, and hence the amount of pulse pile-up and dead time that the digitizer would experience. The detector assembly is held via a clamp attached to the lab stand to ensure that the detector is level with the position of the BeRP ball. The scintillator is coupled with a photomultiplier assembly (Hamamatsu H6559) based on a head-on photomultiplier tube (Hamamatsu R6091), which then connects to a high voltage power supply and digitizer. The high voltage power supply (Ortec 556 HVPS) was set to -1400 V for the duration of the experiments. The digitizer (CAEN DT5730 8-channel, 500 MSps, 14-bit digitizer) was then connected to a laboratory laptop run-

ning CoMPASS software for data acquisition in binary format. The binary data was further processed using custom post-processing software [21]. A fixed 6-dB attenuator was also used to match the output signal with the digitizer input range (0-2V). Once set up, calibration data was gathered using a 800 μCi Cesium-137 (^{137}Cs) source placed 30 cm from the detector with no shielding. The data gathered from this calibration measurement allowed for the identification of the Compton edge of the ^{137}Cs spectrum, located at 80% of the Compton falling edge identified in the spectrum following the procedure described in [13]. Additionally, calibration was repeated before and after measurement to ensure that the detector output remained consistent throughout each experiment.

After calibration, the ^{137}Cs source was removed and replaced with the BeRP ball and the detector setup was moved back to our set measuring distance. Once at the distance, the shielding layers were put in place and the acquisition was started. This calibration and measurement cycle was repeated for each of the four different shielding arrangements. The experimental setup for the shielding arrangement (b) is shown in Fig. 2.1.

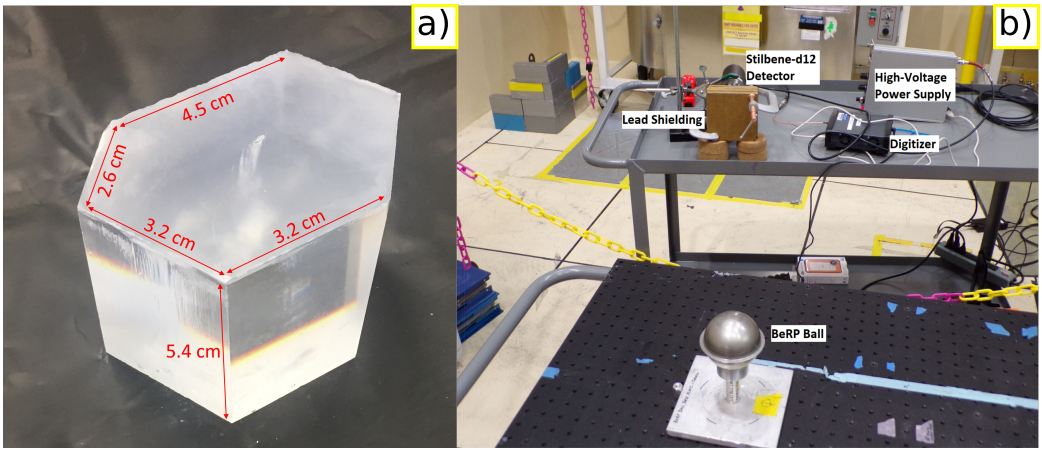

Figure 2.1: Experimental setup at the DAF. This setup uses 5.08 cm of lead shielding placed in front of the detector (configuration (b)), with a distance of 1 meter between the front of the detector and the BeRP ball.

Once the BeRP ball was brought out of its shielded housing and placed onto the staging table, the detector setup was re-positioned to directly face the source. Using the same acquisition settings as the Cesium calibration step, measurements of each of the shielded configurations were performed for one hour of acquisition time, with the total number of detected counts

varying with the type of shielding. For each of the measurements, a source-to-detector distance of 1 meter was used to minimize pile-up while still keeping a reasonable measurement time. A stable background measurement was also acquired for one hour with no sources present in the measurement room. The acquisitions were performed over two separate days, with the first day only having enough time for the unshielded, 5.08 cm PE, and 5.08 cm lead shielding configurations. The second day allowed for the final measurement, a combination of one inch of polyethylene and one inch of lead shielding plates, to be acquired along with a Cesium calibration and a re-measurement of the unshielded configuration to ensure that there would be enough data for accurate analysis. With all of these measurements taken, further processing steps needed to be done to use this data for our intended neutron source unmixing applications and are described in the following section.

2.3 Data Processing

Once all data was collected from the DAF experiments, the pulse information from each of the shielding setups can be processed through a pulse shape discrimination calculation to distinguish between neutron and gamma pulses, as well as eliminate any pile-up pulses that may be present. In order to separate the neutron pulses from the gamma ray pulses in the spectrum, a number of steps must be taken to remove unwanted pulses. Once the neutron spectra is properly separated, the detector response must be characterized so that the neutron energy spectra can be extracted. Lastly, a modified version of our previously demonstrated unmixing algorithm can be used to identify these different spectra from a mix of shielding materials.

2.3.1 Detector Calibration

Prior to all SNM measurements that were performed at the DAF, a calibration step was performed to determine the correlation between light output and incoming particle energy. Unlike inorganic scintillators or semiconductor detectors, radiation detection by organic scintillation mainly relies on Compton scattering (gamma-ray detection) and elastic scattering (fast-neutron) detection because of the light-Z materials present in the detectors. Therefore, calibration needs to be performed using Compton-interaction-specific

features in the detection spectrum. As a consequence, the calibration coefficient relates the energy deposited in electron-equivalent units (ee) to the pulse integral signal, in Volts (V×ns per unit sampling time. This calibration step utilizes the Compton edge of ^{137}Cs on an organic scintillator to relate these two values and get a correlation coefficient in units of $keVee/V$. To perform this measurement at the DAF, a 800 μCi ^{137}Cs source was placed about 1 meter away from the detector front face and the spectra were collected using the stilbene-d_{12} detector. Each of these measurements was performed for between 5 and 10 minutes, allowing plenty of time to distinctly see a Compton edge forming. This location corresponds to the 478 keV Compton edge of the ^{137}Cs spectra, created by the maximum scattered energy of an incoming 661.7 keV gamma-ray. This energy value is calculated using the Compton scattering formula in Equation 2.1.

$$E_{e^-} = E_\gamma - \frac{m_0c^2}{(1 - cos\theta) + \frac{m_0c^2}{E_\gamma}} \tag{2.1}$$

where E'_γ is the recoil gamma energy, E_γ is the incident gamma energy, m_0c^2 is the electron rest mass multiplied by the speed of light squared (0.511 MeV) , and θ is the gamma scattering angle. In the case of a gamma backscatter, the gamma energy would be at a minimum and the resultant deposited energy by the recoil electron is maximum. This occurs when the gamma scattering angle is at 180°. Solving this equation using the 661.7 keV gamma decay energy from ^{137}Cs as the incident gamma ray energy, and a 180° scattering angle, results in energy deposited in the detector by the recoil electron of 478 keVee, hence in electron-equivalent units. This interaction causes the formation of the Compton edge in the detected spectra. As such, finding the point location at which this Compton edge occurs, calculated as the point at 80% of peak maximum along the falling edge of the Compton peak, allows for correlating the pulse integral value of the curve to the light output value in electron-equivalent units [22]. This calibration step assumes a linear detector response, which is a good approximation in the energy range of interest, and was performed before the measurements on each of the days to ensure correct and consistent performance of the detector. An example of the Compton edge location is shown in Figure 2.2 below:

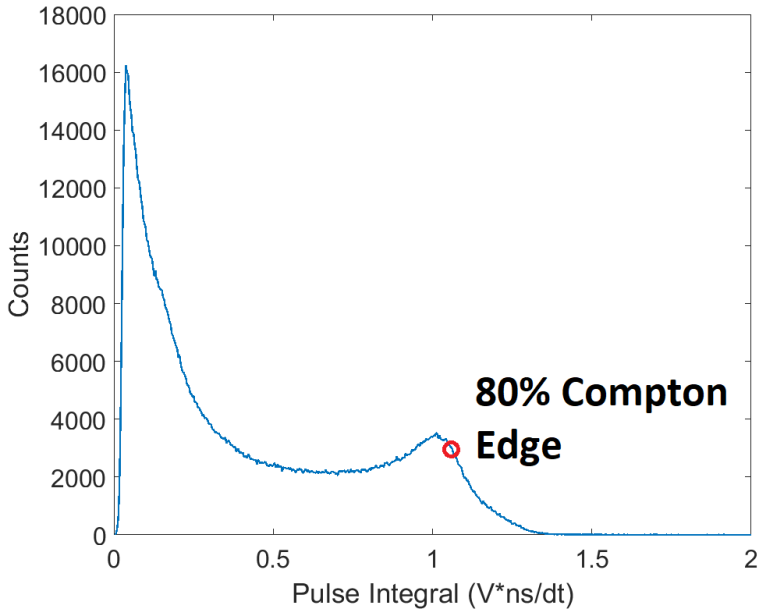

Figure 2.2: Calibration measurement spectra performed at the DAF showing the location of the ^{137}Cs Compton edge.

Performing this calibration using the Compton edge curve shown in Figure 2.2 yielded a calibration coefficient of 434.15 keVee/V. This calibration coefficient can then be used in post-processing steps to convert the measured pulse integral distribution to a light output spectra. Pulse shape discrimination needs to be performed to select neutron-produced pulses and derive the light-output spectrum.

2.3.2 Pulse Shape Discrimination

Pulse shape discrimination (PSD) is a methodology that is meant to distinguish between different detected types of radiation owing to the different shapes of the detected pulses, in the time domain. This is a specific property of a class of organic scintillators. Stilbene-d_{12} exhibits an excellent capability of detecting and discriminating between pulses produced by different types of radiation, through PSD. A quenched light-output response to particles with different ionization densities determines the PSD capability exhibited by organic scintillation detectors. Our detailed characterization of stilbene-d_{12} is reported elsewhere [12]. High linear energy transfer (LET) particles, such as deuteron recoils produced by neutron interactions are highly quenched and exhibit a delayed fluorescence component more prominent than the fast

fluorescence one, when compared to low-LET particles, such as electron recoils produced by gamma-ray interactions. PSD enables the discrimination between different interacting radiation based on the time constants of the fluorescence signal following ionization caused by ions with different LET. Figure 2.3 shows the difference of the pulse shapes in the time domain for template pulses measured from particles with different LET. We used the charge-integration technique [23] to exploit the PSD capability of the detector and discriminate between pulses produced by the interaction of different types of radiation.

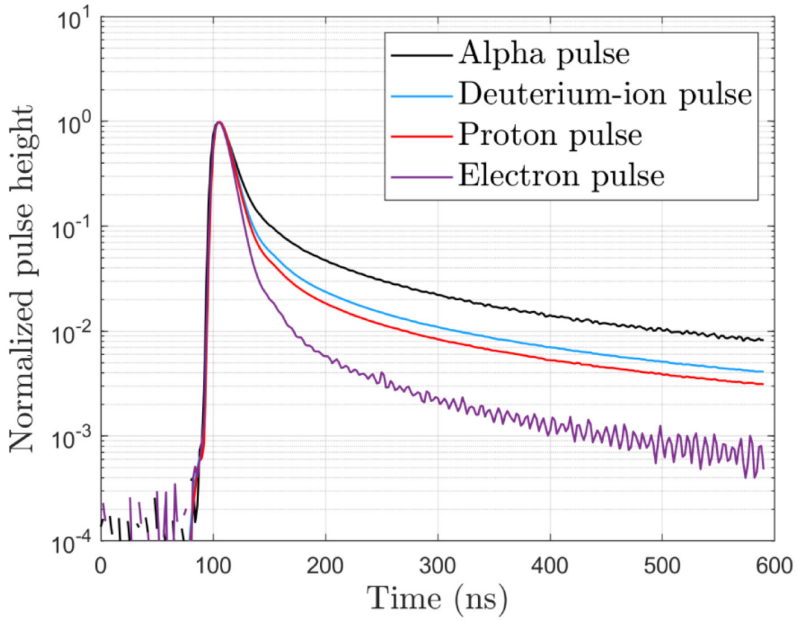

Figure 2.3: Comparison of different pulse types when interacting with the stilbene-d_{12} scintillation crystal [12].

According to this method, each pulse was split into prompt and tail components, and integrated. Neutron pulses exhibit a relatively higher signal in the tail due to the delayed fluorescence, compared to gamma-ray pulses, as expected. A pulse shape parameter, tail-to-total-ratio (TTR), was constructed from an arbitrary ratio of the tail integral to the total pulse integral, and used for PSD. The tail was defined as starting 22 ns after each pulse maximum, while the total was calculated as the area under the pulse, starting 4 ns before the pulse maximum and extending 200 ns after it. These parameters were optimized in a previous study [13] for the stilbene-d_{12} detector, to maximize the separation between the neutron-produced pulses and the

gamma-ray-produced ones. When creating a PSD plot, the TTR is plotted against the light output. Owing to the different pulse shapes, separate bands in the PSD scatter-density plot that correspond to gamma and neutron pulses can be identified, with neutron pulses having a higher tail-to-total ratio, on average. In the presence of a high radiation flux, pulse pile-up may severely affect the pulse discrimination results. In PSD-capable detectors, a piled-up gamma-ray pulse may be incorrectly classified as a neutron pulse because of an increase in the tail integral and hence PSD parameter. In this work, we first filtered piled-up pulses using an algorithm described in the following section and then applied the PSD-based discrimination to identify neutron-produced pulses and generate neutron light-output spectra to be independently analyzed using the unmixing algorithm. A low-light-output threshold of 40 keVee, corresponding to a neutron energy deposited threshold in stilbene-d_{12} of 486 keV was also applied. Figure 2.4 below displays a PSD scatter density plot for the unshielded DAF measurement.

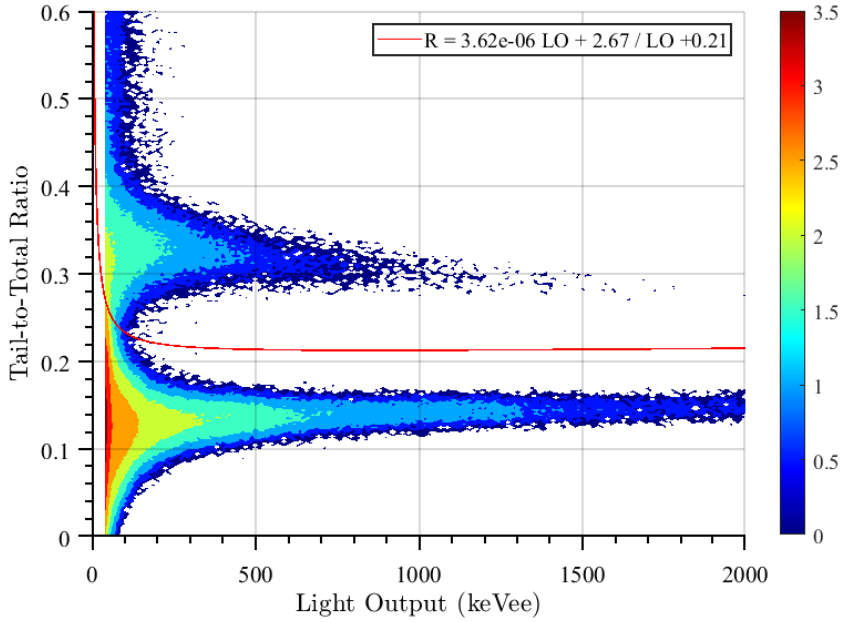

Figure 2.4: Pulse-shape discrimination scatter density plot for the unshielded DAF measurement using optimized parameters. The discrimination line R is shown in red, separating pulses into neutron (above R line) and gammas (below R line).

The number of rejections, neutrons, and gamma pulses were determined using the discrimination line R, as shown in Figure 2.4. The PSD discrimination equation as a function of the pulse light output (LO) R =

3.62×10^{-6}LO+0.21 + 2.67×LO^{-1} was used to select neutron pulses as the pulses featuring a TTR above the discrimination line [13]. Pulses that lie below this R line are classified as gamma pulses. However, if the pulses have a tail-to-total ratio higher than 0.5, they are instead rejected pulse since these pulses are highly likely to be remaining double pulses. Removing any remaining piled-up or double pulses in the data was then done through the use of the pile-up rejection algorithm described in the following section.

2.3.3 Pile-up Rejection

Piled-up pulses can be found when more than one pulse is detected simultaneously, creating a distorted waveform with more than one peak. The probability of two or more particles (n) interacting in the same time window of length τ is given by $P = e^{-\theta\tau}(1 - e^{-\theta\tau})^{n-1}$, where θ is the average count rate in counts per second [24]. For example, for a time window of 592 ns and average count rate of 15,900 pulses per second, which were the acquisition conditions of the unshielded irradiation, the probability of two pulses occurring in a single window is approximately 1%, yielding a double-pulse count rate of approximately 159 counts per second. This probability is not negligible and piled-up pulses should be filtered. The measured fraction of piled-up pulses, after implementing the rejection is approximately 0.7%, in reasonable agreement with the calculated fraction. The waveform in Figure 2.5 shows an example rejected pulse from the unshielded BeRP ball data, with the waveform having a clear smaller secondary peak directly after the primary peak.

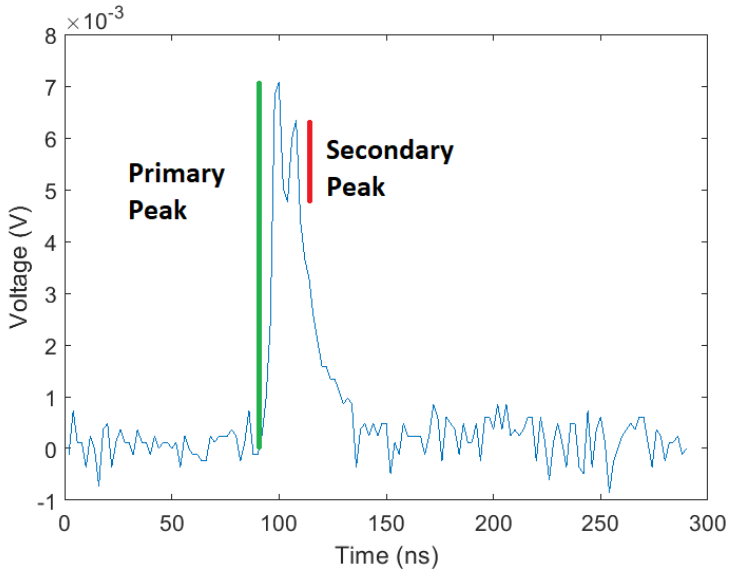

Figure 2.5: A pulse waveform classified as rejected by the pile-up rejection algorithm.

Extending the approval and rejection process to all pulses detected during the acquisition allows for the creation of a PSD scatter density plot. Shown below in Figure 2.6 is a PSD plot comparison before and after the introduction of a pile-up rejection calculation for the unshielded BeRP ball experiment:

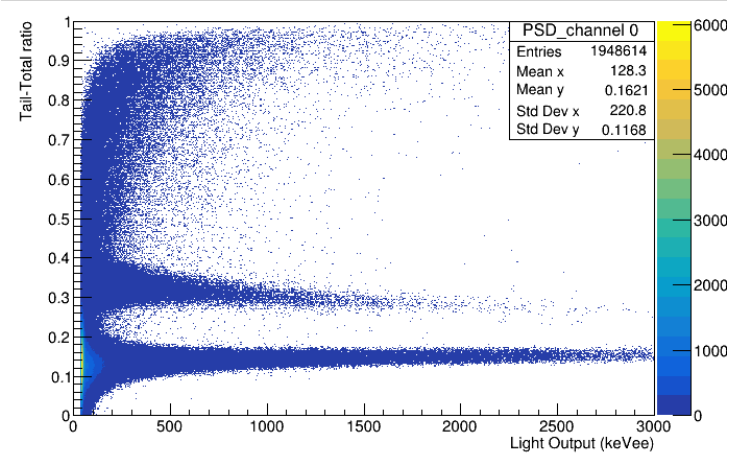

(a) Pulse shape discrimination graph without pile-up rejection

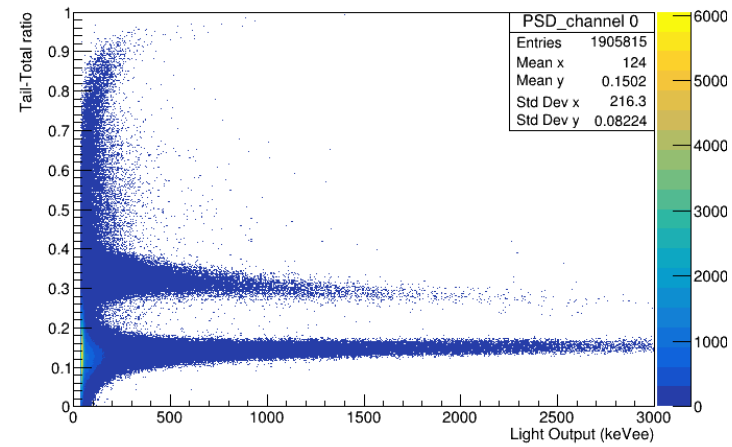

(b) Pulse shape discrimination graph with pile-up rejection

Figure 2.6: Comparison between cleaned and uncleaned pulse shape discrimination plots for the unshielded BeRP ball detection scenario.

As shown in Figure 2.6, the addition of pile-up rejection greatly reduces the number of pulses in the high light output and high TTR range. Without the addition of the PUR algorithm, these pulses would likely be classified as neutrons during PSD. The PUR algorithm instead analyzes the waveform of each pulse and looks for secondary peaks that can be classified as piled-up pulses, then uses a set of parameters to determine if the pulse is accepted or rejected.

The rejection technique classified pulses as piled-up if consecutive samples increased by an amount that exceeded a set fraction of the pulse amplitude, defined as minimum peak ratio (MPR). For example, if the threshold is

set at 0.1, then any waveform with a secondary peak with an amplitude above baseline greater than 0.1 times the primary peak amplitude will be rejected. This calculation can be illustrated with the peak heights shown for the primary peak and secondary peak in Figure 2.5, where the relative height of this secondary peak in red is compared with the height of the primary peak in green. However, this technique also rejects low-amplitude pulses that do not exhibit pile-up, but only noise in the tail region. We improved this method to maximize the amount of rejected piled-up pulses while retaining low-amplitude pulses, by adding an additional parameter. This parameter sets a minimum height of the secondary peak for rejection, called minimum peak height (MPH). Having too low of a MPH may remove too many pulses with small secondary peaks, whereas too high of an MPH may allow too many potential double pulses that are not rejected by the MPR to be accepted.

In this work, we measured the detector neutron intrinsic efficiency to a fission spectrum in a field at a low fluence rate, i.e., with negligible pile up rate, and optimized the MPR and MPH in the unshielded BeRP measurement to reject piled-up pulses while keeping a detection efficiency comparable to the reference one. Visual inspection of the PSD plot also helped to determine the effectiveness of the pile-up rejection algorithm. The rejection fraction as a function of these parameters is shown in Table 2.1 below.

Table 2.1: Rejection Fraction testing to determine the optimal pulse-shape discrimination parameters using the unshielded BeRP ball measurements. Neutron rejection fraction (NRF) is shown as an increasing fraction, showing how a greater proportion of the neutrons are rejected as the MPH value decreases.

MPH	**Neutrons**	**Rejections**	**NRF**	**Detection Efficiency**
0.5	326448	0	0	37.4±0.2%
0.15	326448	0	0	37.4±0.2%
0.1	326416	50	9.619E-05	37.4±0.2%
0.05	325995	512	0.0014	37.4±0.2%
0.025	324160	2611	0.0070	37.2±0.2%
0.01	314285	13103	0.0373	36.0±0.2%
0.008	309440	17819	0.0521	35.5±0.2%
0.006	**300260**	**25846**	**0.0802**	**34.4**±0.2%
0.004	277151	42794	0.1510	31.8±0.2%
0.002	143347	113486	0.5609	16.4±0.3%

The optimized parameters were: minimum peak ratio of 0.005 and a minimum peak height of 0.006. These parameters give a neutron rejection fraction of 8.02% while maintaining a neutron detection efficiency of 34.4±0.2%, which is as close to the intrinsic fission efficiency of 33.6±1.0% calculated in our reference data set as we could reasonably achieve without rejecting too many neutrons. Our reference data set was created using a 5 μCi californium-252 fission source and the stilbene-d_{12} detector set up in the same manner to the experiments performed at the DAF. The source was placed 50 cm away from the front face of the detector. Performing PSD on the data shown in Figure 2.7 allows us to extract the pulse integral distribution (PID). The area of the PID corresponds to detected neutrons. The intrinsic efficiency was calculated as in Equation 2.2:

$$\varepsilon_{int} = \frac{N_{meas}}{S \times \Omega} \tag{2.2}$$

where N_{meas} is the number of neutrons measured by the detector, while S the source strength, i.e., the number of radiation quanta emitted by the source and Ω the solid angle. The number of neutrons measured by the de-

tector is obtained through the PSD calculation, while the number of neutrons impinging on the detector can be calculated through a solid angle approximation for the ^{252}Cf reference experiment.

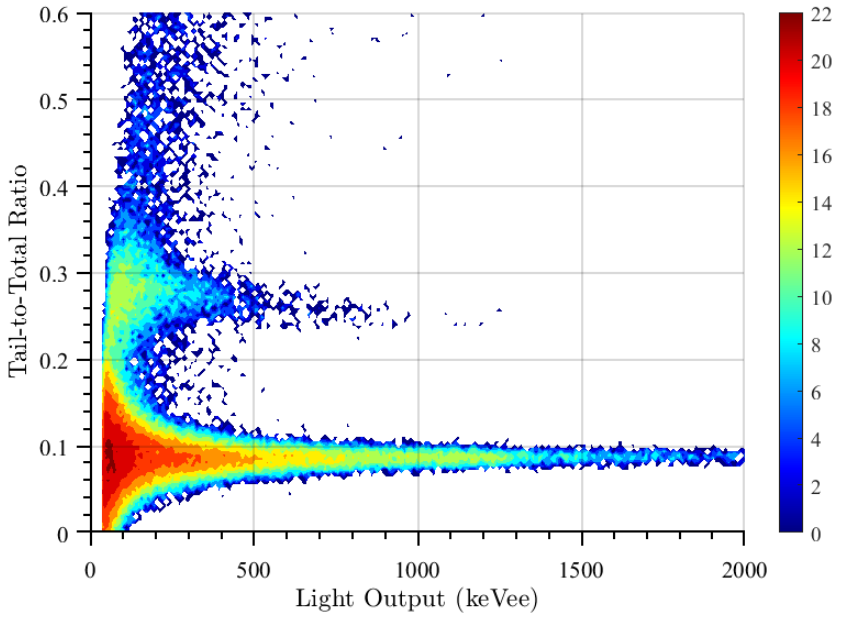

Figure 2.7: Pulse-shape discrimination scatter density plot for the reference ^{252}Cf experiment to calculate the efficiency of the stilbene-d_{12} detector on a fission source.

This intrinsic efficiency of 33.6±1.0% was then used for comparison with the efficiencies calculated in Table 2.1 to find the optimal parameters that correspond to a comparable efficiency. The source strength in the BeRP ball irradiation was calculated via simulation, using the model described in Section 2.4. These parameters were applied to process the data of all the shielding configurations. Separating the neutron pulses from this data set allows for the creation of a light output spectrum solely based on the stilbene-d_{12} light output of neutron-classified-pulses. These measured neutron light output spectra were used to validate simulated neutron light output spectra. This step allowed for the experimentally-validated simulated light output spectra to be implemented into the unmixing algorithm for identification of the shielding material.

2.4 MCNP Simulation

We created a simulated model of the experimental setup at the DAF to validate the unmixing algorithm on well-controlled data with minimum experimental uncertainties, both systematic and stochastic, and to test several configurations that were not measured. The simulated BeRP ball matches its known isotopic composition at the time of measurement [11]. Additionally, the BeRP ball simulation accounts for both induced and spontaneous fission for the isotopic composition of the stainless-steel cladded plutonium sphere. The BeRP ball has a relatively high plutonium-240 mass fraction (5.9%), leading to a very high number of spontaneous fissions occurring within its geometry [11]. For comparison, plutonium-240 has a spontaneous fission rate of approximately $1.6\times10^{6}\ \frac{fissions}{g*hr}$ while plutonium-239 has a spontaneous fission rate of approximately 40 $\frac{fissions}{g*hr}$ [25]. The simulation was performed using MCNPX-PoliMi, which records the event-by-event interactions with the detector cell and incorporates, in its associated post-processing code MPPost, the detector's light output response for a seamless simulation of the light output spectrum. Combining the information gathered in these simulations with the data gained in the physical experiments creates a more comprehensive view of the detection scenario that can provides a comprehensive dataset for the unmixing and unfolding algorithms.

2.5 Unmixing Algorithm

The unmixing calculation uses a Bayesian algorithm to find the mixing coefficients associated with elements in a reference library to assess their contribution to the measured spectrum. In previous studies, several Bayesian approaches were analyzed to solve this problem [26, 27]. These methods exploit the posterior distribution of the mixing coefficients, by combining the observed data with available prior information. We have observed that a sparsity-promoting approach using a Bernoulli-truncated Gaussian (BTG) prior model yielded accurate estimates for the nuclide fractions in the unknown mixtures [27] and, therefore, we only consider this method in this work.

Given a light output spectrum $\mathbf{y} = [y_1, \ldots, y_M]^T$, observed in M light output bins, which is associated with a mixture of up to N known configurations,

whose individual spectral responses are denoted by $\{\mathbf{A}_{:,n}\}_{n=1,\ldots,N}$ and gathered in the $M \times N$ library matrix $\mathbf{A} = [\mathbf{A}_{:,1}, \ldots, \mathbf{A}_{:,N}] = [\mathbf{A}_{1,:}^T, \ldots, \mathbf{A}_{M,:}^T]^T$. Each $\mathbf{A}_{m,:}$ is a row vector gathering the spectral responses of the N known elements to be unmixed in the mth light output bin. The coefficient associated with the nth element to be unmixed, corresponding to the amount present in the mixture, is denoted by x_n and the N coefficients are gathered in the vector $\mathbf{x} = [x_1, \ldots, x_N]^T$. In this work, $N = 4$ since we included the three different shielded BeRP ball configurations and the one unshielded configuration measured at the DAF. At a first approximation, we assume a linear mixing model of the possible components, which can be expressed in matrix form as $\mathbf{y} \approx \mathbf{A}\mathbf{x}$. $\mathbf{A}$ is known and is omitted in all the conditional distributions hereafter. As mentioned above, the observation noise is modeled by Poisson noise, leading to the following form of the likelihood

$$f(y_m|\mathbf{x}) = (\mathbf{A}_{m,:}\mathbf{x})^{y_m} \exp\left[-\mathbf{A}_{m,:}\mathbf{x}\right]/y_m!, \quad \forall m = 1, \ldots, M. \tag{2.3}$$

The entries of $\mathbf{y}$ are independently distributed, i.e., $f(\mathbf{y}|\mathbf{x}) = \prod_{m=1}^{M} f(y_m|\mathbf{x}) = \prod_{m=1}^{M} f(y_m|\mathbf{A}_{m,:}\mathbf{x})$ and are conditioned on the value of $\mathbf{x}$. Bayesian methods rely on the knowledge of prior information available about $\mathbf{x}$, the coefficients, to enhance their recovery from the observable $\mathbf{y}$, the light output spectrum. The a-priori information is the prior distribution $f(\mathbf{x})$ and the estimation of $\mathbf{x}$ can then be achieved using the posterior distribution $f(\mathbf{x}|\mathbf{y}) = f(\mathbf{y}|\mathbf{x})f(\mathbf{x})/f(\mathbf{y})$.
The efficient sparsity-promoting BTG prior model of $\mathbf{x}$ is described in Eq. (2.4)

$$\begin{aligned} f(x_n|w_n) = (1 - w_n)\delta(x_n) + w_n\mathcal{N}_{\mathbb{R}^+}(x_n; 0, \sigma_n^2), \quad \forall n = 1, \ldots, N \\ f_n(w_n = 1) = \pi_n, \quad \forall n = 1, \ldots, N, \end{aligned} \tag{2.4}$$

In Eq.(2.4), $\delta(\cdot)$ denotes the Dirac delta function, which is equal to 1 when $x_n = 0$ and 0 elsewhere and where $\mathcal{N}_{\mathbb{R}^+}(x_n; 0, \sigma^2)$ is a probability density function (p.d.f.) truncated Gaussian distribution, defined on $\mathbb{R}^+$ to enforce the non-negativity of the elements of $\mathbf{x}$. The truncated Gaussian prior has hidden mean 0 and hidden variance σ^2these are the mean and variance of the non-truncated Gaussian distribution). The presence of the nth element is controlled by the binary variable w_n, which is equal to 1 when the nth is

present and 0 otherwise. π_n is the prior probability of presence of the nth element.

We set $\pi_n = 1/N, \forall n$ as we expect a limited number of possible elements to be simultaneously present in the mixture, while we do not wish to promote any specific element. These parameters can however modified by the practitioners. We set the variances $\{\sigma_n^2\}$ as in Eq. (2.5) for each element

$$\sigma_n^2 = 0.1 \sum_{m=1}^{M} y_m. \tag{2.5}$$

Instead of considering a prior model only for $\mathbf{x}$, Eq. 2.4 defines a joint prior model for $(\mathbf{x}, \mathbf{w})$, where $\mathbf{w} = [w_1, \ldots, w_N]^T$, expressed as $f(\mathbf{x}, \mathbf{w}) = \prod_{n=1}^{N} f(x_n|w_n) f_n(w_n)$. The proposed unmixing algorithm thus aims at estimating jointly $(\mathbf{x}, \mathbf{w})$, i.e., at performing jointly the element identification (through $\mathbf{w}$) and quantification (through $\mathbf{x}$).

Using the Bayes' rule, the joint posterior distribution of $(\mathbf{x}, \mathbf{w})$ is given by $f(\mathbf{x}, \mathbf{w}|\mathbf{y}) = f(\mathbf{y}|\mathbf{x}) f(\mathbf{x}, \mathbf{w}) / f(\mathbf{y})$.

The algorithm adopted in this work and originally described in [27] relies on approximate Bayesian estimation and builds an approximate distribution $Q(\mathbf{x}, \mathbf{w}) \approx f(\mathbf{x}, \mathbf{w}|\mathbf{y})$ whose moments are much simpler to evaluate than those of $f(\mathbf{x}, \mathbf{w}|\mathbf{y})$. The method belongs to the so-called class of expectation propagation (EP) methods [28] to provide approximate point estimates of the mean and the covariance of the posterior distribution of $\mathbf{x}$ (and $\mathbf{w}$). It offers several advantages compared to traditional approaches that exploit the posterior distribution using Hamiltonian Monte Carlo methods [26, 29] and is also motivated by the fact that the posterior means $E_{f(\mathbf{x},\mathbf{w}|\mathbf{y})}[\mathbf{x}]$ and $E_{f(\mathbf{x},\mathbf{w}|\mathbf{y})}[\mathbf{w}]$ associated with the posterior distribution $f(\mathbf{x}, \mathbf{w}|\mathbf{y})$ are intractable analytically. Further details on the EP algorithm and its implementation can be found in our previous work [27] and are available online in its current version at [30].

2.5.1 Unmixing Application

Our previously demonstrated unmixing algorithm can be used to identify the shielding materials of the shielded neutron spectra acquired at the DAF. The first part of my work on the unmixing algorithm was to show the effectiveness

of this algorithm in the identification of mixed radioisotopes in the presence of a varying background signature [4]. However, this detection scenario presents a new challenge for the algorithm: finding an unknown shielded neutron spectra's identity where the shielding material is the primary determinant of the spectral differences between library components.

2.5.2 Demonstration of Unmixing for Gamma-ray Spectra

The unmixing algorithm utilizes two input datasets: 1) a spectra library that contains all possible components of a mixed spectra, and 2) the spectra that the unmixing will be performed on. The spectra library in in the first part of this work uses all of the possible spectra of gamma decay radioisotopes that could be measured as well as a standard background measurement [4]. Source spectra were acquired using an EJ-276 plastic scintillator detector on each of the available laboratory sources in order to test the algorithm with mixtures of widely varying spectra. Additionally, a series of background measurements were taken outdoors to measure any possible weather-caused differences in the background spectra, thus allowing us to confirm the adaptability of this algorithm to varying weather conditions. A scaled amount of Poisson noise was then added to the tested mixtures to account for additional statistical variation in each measurement. The mixture spectra was then run on the algorithm to produce two outputs: 1) The predicted presence probability of each of the isotopes in the library, and 2) the predicted proportional amount of each isotope that could be present in the mixture. Figure 2.8 below shows an example library of gamma-ray emitting radioisotopes that was used for testing the unmixing algorithm.

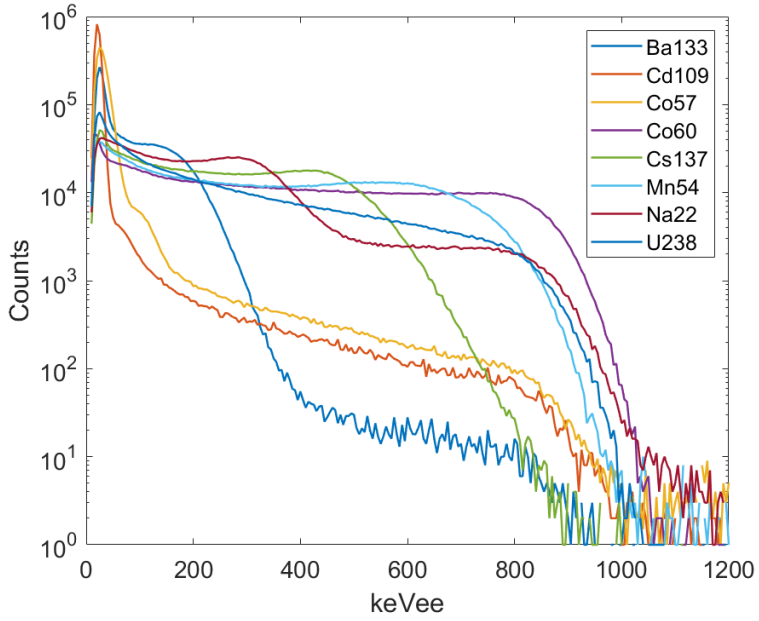

Figure 2.8: Gamma-ray emitting radioisotope library used as input to the unmixing algorithm. Measurements were taken using an EJ-276 plastic scintillator detector to acquire distinct spectra shape for each isotope.

As shown in Figure 2.8, each radioisotope has a different light output spectra that can be identified by the unmixing algorithm. For example, if a mixture contained 1-part ^{137}Cs and 1-part ^{60}Co, the algorithm would predict a 99.9% presence probability for both ^{137}Cs and ^{60}Co and minimal to zero percent chance for the others. Additionally this example would produce a predicted proportional amount of around 0.5 for ^{137}Cs and 0.5 for ^{60}Co, showing that it predicts the mixture to be made up of 50% ^{137}Cs and 50% ^{60}Co. This process of Poisson randomization and running is repeated many times to then create an average for the predicted amount of each isotope, predicted presence probability for each library component, and the associated uncertainty. A heatmap showing the predicted presence probability for a mixture of radioisotopes can be seen in Figure 2.9 below:

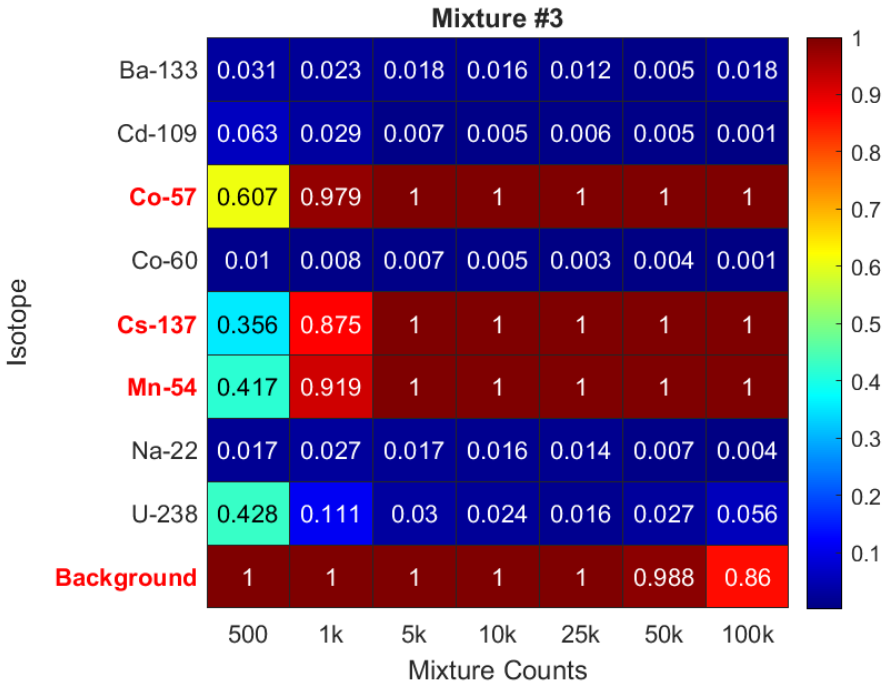

Figure 2.9: Unmixing results from a mixture of ^{137}Cs, ^{57}Co, ^{54}Mn and background signal. The number displays the average predicted presence probability from the unmixing algorithm for each isotope from 0 to 1, with 1 indicating 100% presence probability.

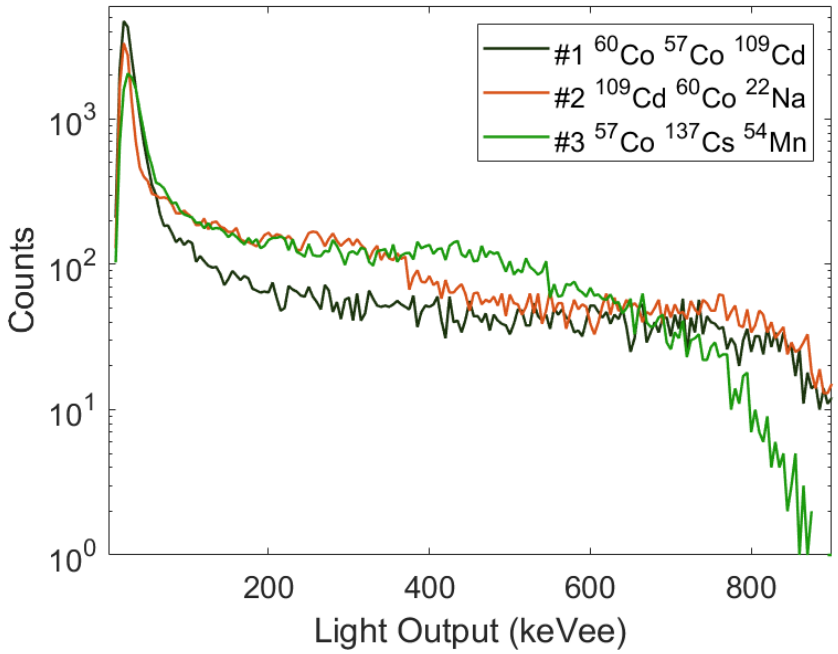

Figure 2.10: Three different mixture light output spectra tested with the unmixing algorithm.

Figure 2.9 shows how the unmixing algorithm can effectively identify the unknown components of the mixture both accurately and consistently [4]. The x-axis on this plot displays the number of mixture counts, with more mixture counts allowing for a more clearly defined spectra and lower impact of the Poisson noise on overall shape. At very low mixture counts, the algorithm has trouble distinguishing between similar radioisotope spectra, but at around 5000 total mixture counts the algorithm can accurately predict which isotopes are present. The tested mixtures shown in Figure 2.10 show how the spectra of these mixtures are all relatively similar, in overall shape and scale. Even with the lack of significant variation, the unmixing algorithm was able to effectively identify each of the mixture's components at around 5000 total mixture counts. With the success of the gamma decay radioisotope spectra unmixing, this algorithm can be expanded for use on neutron spectra which tend to be more similar in shape.

2.5.3 Detector Response Characterization

A high-fidelity simulation model of organic scintillation detectors needs to incorporate the material-specific light quenching parameters to output the light output spectrum, given the energy deposited via neutron scattering by deuteron recoils. The light output response of stilbene-d_12 was measured using a DT neutron generator in a scatter-based experiment at NML.

The experiments to characterize the light output response began with a similar detector calibration step to the DAF experiments, where a ^{137}Cs source is used to determine the corresponding channel number to the Compton edge of the ^{137}Cs spectra. The detector was then placed 120 cm away from a deuterium-tritium (D-T) generator and it was used as a scattering medium for characterization measurement [12]. Two EJ-309 detectors (5.08cm diameter by 5.08 cm length) were placed at various angles to measure the scattered 14.1 MeV neutrons originally produced by the deuterium-tritium interaction after their interaction with the stilbene-d_12. A schematic displaying this setup is shown in Figure 2.11. Since the primary neutron energy and scattering angles were known based on the detector placement, the energies of the scattered deuterium ions in the detector and scattered neutrons were known. Through a time-of-flight setup and the application of a time gate between the start and stop detectors, true scattering events

were discriminated from accidental coincidences within the short time gate window.

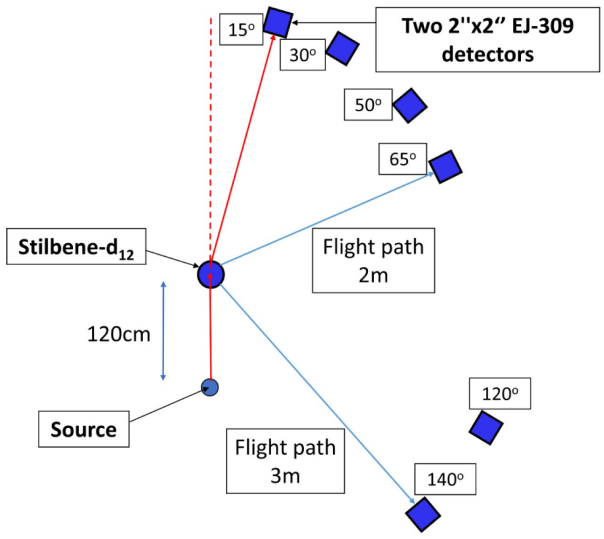

Figure 2.11: Schematic showing the light output characterization setup for the stilbene-d_{12} detector.

We hence measured the stilbene-d_{12} light output values corresponding to the energies deposited by the scattered deuterium ions of known energy. These measurements were done at six different scattering angles (15°, 30°, 50°, 65°, 120°, 140°), shown in Figure 2.11, each of which were chosen based on the relatively large scattering differential cross section. These light output values were then used to fit the semi-empirical Birks model, shown in Equation 2.6, which describes the light quenching through the parameter B.

$$LO(E) = \int_0^{E'} \frac{AdE}{1 + B(dE/dr)} \tag{2.6}$$

Equation 2.6 also must consider the particle stopping power in the scintillation materials, dE/dr, and the scintillation efficiency, A. The Birks equation parameters A and B were found through the fitting of the Birks curve on the LO response data acquired at each of the experimental angles. The fitted Birks curve for the deuterium-ion data results in an A value of 0.75 $\pm$0.05 ($\frac{MeVee}{MeV}$) and a B value of 5.80 $\pm$0.10 ($\frac{mg}{MeV*cm^2}$). Figure 2.12 shows the LO response as a function of deuteron-deposited energy.

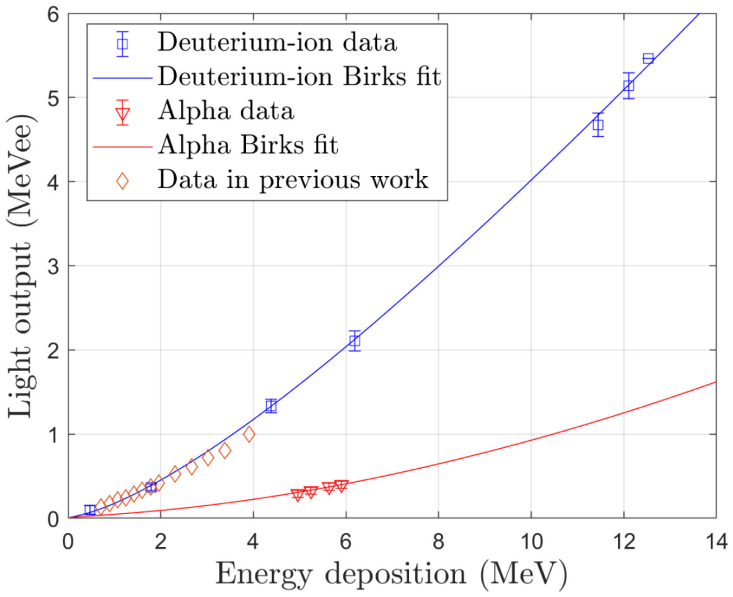

Figure 2.12: Light output conversion curve showing the relationship between the energy deposition and the light output for both deuterium-ion and alpha particle interaction [12].

The measured light output response is used by MPPost to produce light-output spectra, given the Monte-Carlo simulated energy deposited. Individually this can be used for the conversion of neutron energy at the specified energy level to the light output. However, when combined in a matrix with the spectra for each neutron energy from 0.1 MeV to 20 MeV, the light output response matrix can be created. This matrix is a very powerful tool that has a variety of uses for many different applications of the stilbene-d_{12} detector. For this experiment, this response matrix is needed by our unfolding algorithm in order to derive the most-likely energy spectrum that produced a measured light-output spectrum, i.e., to perform neutron spectroscopy. This generated response matrix is shown in Figure 2.13 below:

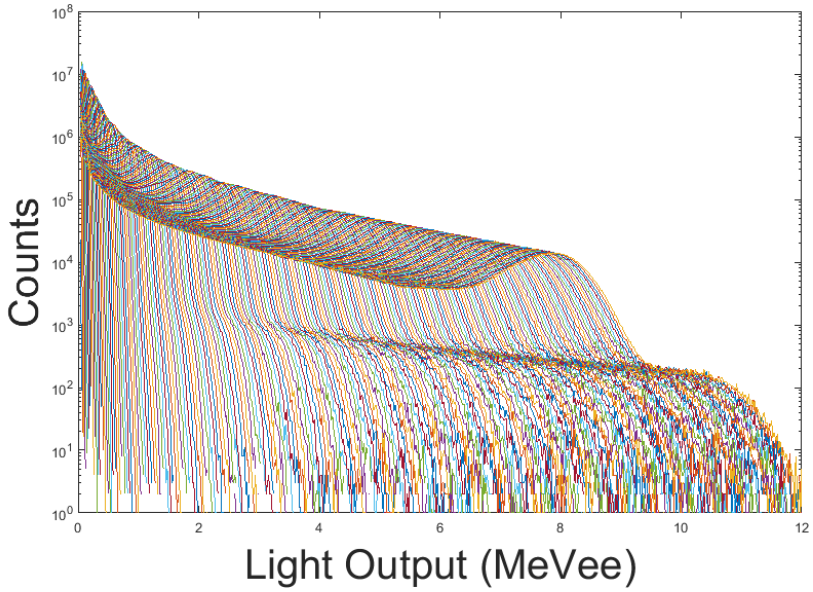

Figure 2.13: stilbene-d_{12} scintillation crystal response matrix plot with a log-scaled y-axis. Each individual line represents a different incident neutron energy from 0.1 to 20 MeV for a total of 200 lines.

2.6 Cross-section-modified Spectra Library Method

The current shielded stilbene-d_{12} light output spectra can be effectively distinguished between and identified by using a well-established library of existing light-output spectra using the tested shielding materials. However, in a more realistic scenario, it is unlikely that such a well-established library with many tested shielding materials would be available for use, so finding a solution that can overcome this issue is desirable for field applications. The possibility that I have explored is the use of material cross section combined with the unmixing algorithm to predict how a modified spectra would appear when attenuated with shielding material. The main determining factor in the shielded spectra that differentiates it from the other materials spectra is the cross section that is specific for that material composition. As neutrons are incident upon the the shielding plate, they are attenuated by the material to scatter and slow down in proportion with the material cross section. The materials that were used for our experiments each have a unique cross-section signature such as those shown in Figure 2.14 below:

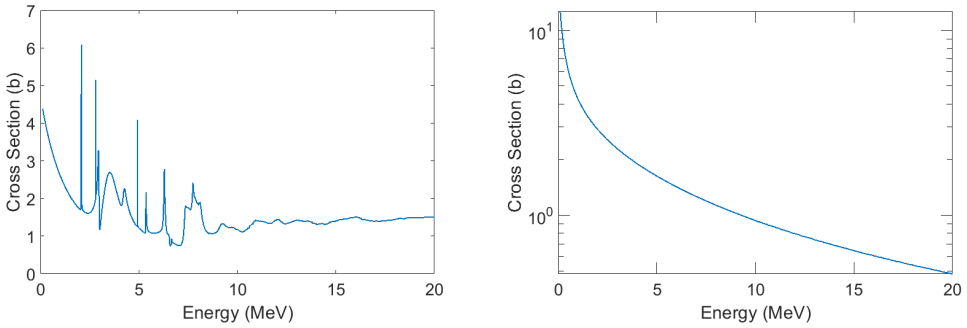

(a) Natural carbon total neutron cross section as a function of energy (MeV)

(b) Hydrogen total neutron cross section (in log scale) as a function of energy (MeV)

Figure 2.14: Comparison between cross section plots for two different materials, carbon and hydrogen. These two combined are the components of the polyethylene shielding material.

As shown in Figure 2.14, at the energy range for the light output calculation for the detector of 0.1 to 20 MeV, there is large variation between the cross section of each material. The cross section at each energy level can then be applied to an unshielded spectra to predict how the overall spectra would change from this attenuation. The equation for the attenuation of the spectra as a result of shielding is shown in Equation 2.7 below:

$$\phi_j^{mod} = W_j \prod_l \exp\left(-\sigma_{lj}\tau_l\right) \tag{2.7}$$

This simplified approximation can be taken since the detector is sensitive to only to fast neutrons hence the neutron thermalization process can be neglected. In Equation 2.7, τ represents the 5.08 cm shielding thickness, l represents the material isotope, j represents the energy bin, σ_{lj} represents the cross section of the material at a specific energy, and W_j represents the BeRP ball spectra at a specific energy group. The resultant ϕ_j^{mod} represents the modified spectra at a specific energy group, where the combination of all of these energy groups create the predicted shielded spectra for this material. In the case of polyethylene where the material is a combination of carbon and hydrogen, the cross section used is a combination of the cross section of each isotope in proportion with the chemical formula of polyethylene (C_2H_4). A library of these modified spectra can them be used as the library for the unmixing algorithm, where the spectra that will be compared against the library are the neutron spectra acquired in the DAF experiments. To get

these spectra in a comparable form of a neutron energy spectra rather than light output, the light output spectra must be unfolded with the previously generated response matrix (Figure 2.15) to find the neutron energy spectra incident on the detector.

2.6.1 Unfolding Calculation

The unfolding process essentially allows for a light output spectra to be converted to the incident spectra based on the light output response matrix for that detector. The calculation for performing this conversion begins with the Fredholm Integral Equation shown in Equation 2.8 below:

$$y(E') = \int_0^\infty R(E', E)\phi(E)dE \tag{2.8}$$

Equation 2.8 can then be approximated by the linear equation:

$$\mathbf{y} \approx \mathbf{R}\boldsymbol{\phi} \tag{2.9}$$

Where $\phi(E)$ defines the neutron spectrum from a neutron source that is to be measured by an organic scintillator, $y(E')$ is the light output response of the detector, and $R(E', E)$ is the response matrix of the detector to monoenergetic neutrons. In this simplification, each spectrum is discretized into a number of bins. This simplification defines $\boldsymbol{\phi} = [\phi_1, \ldots, \phi_N]^T \in \mathbb{R}_+^N$ which denotes the neutron spectrum discretized over N energy bins, $\boldsymbol{y} = [y_1, \ldots, y_M]^T \in \mathbb{R}_+^M$ which denotes the light output spectrum discretized over M bins, and $\mathbf{R}$ is the $M \times N$ response matrix of the detector. An iterative Bayesian unfolding method was used to derive the neutron spectrum from the measured light output spectrum. The spectrum is found by combining the guess of the previous iteration with the smoothing parameter δ in each iteration. This process is shown mathematically in Equation 2.10 below and in previous work [31].

$$f(\boldsymbol{\phi}, \delta|\mathbf{y}) = \frac{f(\mathbf{y}|\boldsymbol{\phi})f(\boldsymbol{\phi}|\delta)f(\delta)}{f(\mathbf{y})} \propto f(\mathbf{y}|\boldsymbol{\phi})f(\boldsymbol{\phi}|\delta)f(\delta) \tag{2.10}$$

In Equation 2.10, $f(\mathbf{y}|\phi)$ is the probability of observing light output $\mathbf{y}$ from the incident spectrum ϕ, $f(\phi|\delta)$ is the prior distribution, and $f(\phi, \delta|\mathbf{y})$ is the current iterative distribution. The initial guess of the algorithm is set to $\phi^{(0)} = 1$ in the first iteration. Sampling of the neutron spectrum was done using a Markov-Chain Monte Carlo (MCMC) technique, approximated as the posterior mean of ϕ:

$$\hat{\boldsymbol{\phi}} = 1/(N_{iter} - N_{bi}) \sum_{k=N_{bi}+1}^{N_{iter}} \phi^{(k)} \tag{2.11}$$

In Equation 2.11, N_{iter} is the number of iterations, N_{bi} is the initial number of burn-in iterations, and k is the iteration number. The marginal posterior mean $\hat{\phi}$ is approximated by averaging the generated spectra after having removed the first N_{bi} iterations. The N_{bi} corresponds to the burn-in period of the sampler, which is set to 20% of N_{iter}. A marginal 95% credible interval for each element of $\hat{\phi}$ is also calculated as the quantile of the elements in the sampler for the 95% cumulative probability.

Iterations ended when the absolute value of the relative difference between the measured light output and the convolution between the estimated neutron spectrum and the detector's response matrix was lower than 2%. For the case of the BeRP ball shielded spectra using the stilbene-d_{12} response matrix, approximately 600 iterations were required.

Performing this calculation on the simulation-obtained light output spectra for each of the shielding configurations, along with using the calculated response matrix for the stilbene-d_{12} detector, gives a varying neutron source spectra. Each of these spectra have minor differences from one another caused by the variation in shielding material and cross section. The unfolded spectra are shown in Figure 2.15 below:

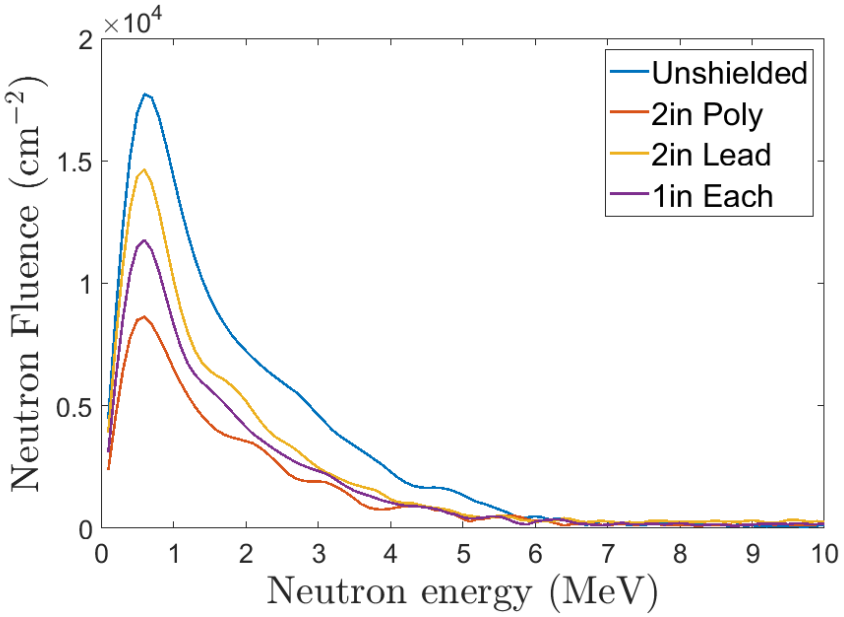

Figure 2.15: Unfolded simulated neutron spectra from each of the DAF shielding scenarios.

As shown in Figure 2.15 above, the unfolding algorithm is able to accurately recreate the initial neutron spectra incident on the detector. Although there appears to be some additional peak variation that occurs along the unfolded neutron spectra, this can largely be attributed to the sampling methodology and corresponds to energy intervals with high associated uncertainty. The shape and magnitude of the peaks relative to one another is consistent with the cross sectional differences and thicknesses for each of the materials. With these spectra properly unfolded, the next step of applying the unmixing algorithm to compare these unfolded results with the cross-section modified spectra library can be performed.

2.7 Source Identification and Confirmation

The following tests were performed, with each varying the two algorithm inputs, to analyze the ability for the unmixing algorithm to determine the identity of the shielding materials. The input data to be unmixed always includes configurations of shielding materials tested at the DAF.

1. **Simulated light output spectra.**

2. **Calculated neutron spectra using the attenuation equation and cross-section of shielding materials.**

3. **Unfolded neutron energy spectra.**

4. **Unfolded neutron energy spectra with calculated spectrum library:**

   (a) **Input:** Neutron energy spectrum created by unfolding the simulated light output spectra for the DAF measurement configurations, Poisson noise added.

   (b) **Library:** Calculated neutron spectra using the attenuation equation and cross-section of various materials including those used for shielding.

2.7.1 Simulated LO Spectra

The first test of the unmixing algorithm was designed to confirm the algorithm's ability to distinguish between simulated stilbene-d_{12} light output spectra, with the only difference between simulations being the BeRP ball shielding material. Shielding materials modulate the neutron spectrum emitted by the BeRP ball in differing ways based on the material composition. Figure 2.16 shows the simulated spectra impinging on the detector front face, after being filtered by the measured configurations. As expected, polyethylene increases the thermal and epithermal relative spectral fractions because of the high scattering cross section of hydrogen and the high fraction of energy retained by proton recoils upon hydrogen-neutron scattering reaction. However, organic scintillators are sensitive to fast-neutrons with a detection threshold of 486 keV. The shapes of the shielding spectra are much more similar at energies above 486 keV, hence unmixing the shielding components in the detector sensitivity energy range is challenging. Prior to the 10^{-4}MeV region of the plot, not shown in Figure 2.16, the spectra is relatively stable before reaching a peak in the thermal energy region.

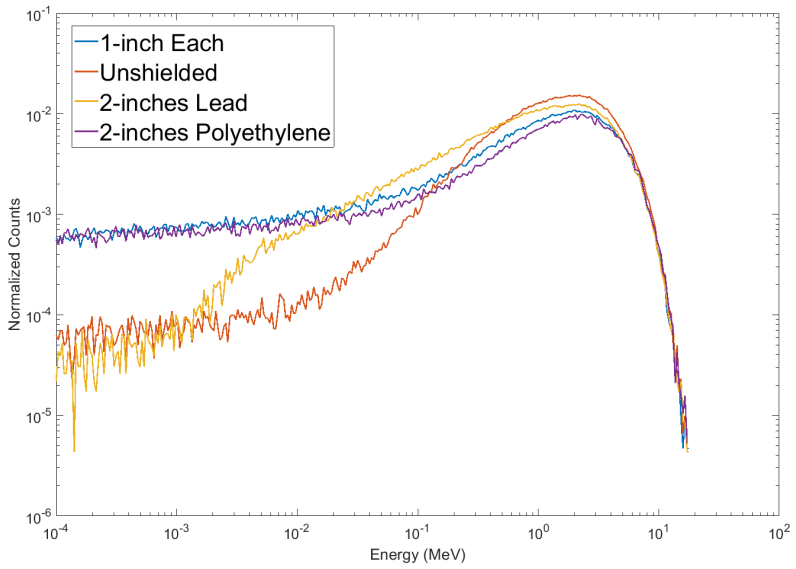

Figure 2.16: Normalized neutron flux spectra for each of the simulated shielded BeRP ball DAF experiments with both axes in log scale.

The stilbene-d_{12} detector composition used in these simulations is sensitive to fast neutrons, hence to the high-energy portion of the spectrum in Figure 2.16. The light-output spectrum retains part of the information on the interacting neutron energy, because the energy of the recoil deuteron is related to the energy of the interacting neutron (Eq. 2.12), where E_n and E_r are the energies of the interacting neutron and the recoil nucleus, respectively. A is the mass number of the target nucleus and θ is the neutron scattering angle. If the neutron is back-scattered, i.e., the recoil deuteron is forward-scattered $\theta = \pi$, and A=2, $E_r = 8/9 \times E_n$.

$$E_r = E_n \times (1 - [\frac{cos\theta + \sqrt{A^2 - sin^2\theta}}{A+1}]^2) \tag{2.12}$$

Additionally, the fore-back asymmetry of n(d,d')n' scattering produces distinct peaks in the light-output response to monoenergetic neutrons. This property results in the favorable neutron spectroscopy capabilities of stilbene-d_{12} and deuterated scintillators in general. Because the light output spectrum partially retains the energy of the interacting neutron, we applied the unmixing algorithm directly to the measured light-output spectra measured under different shielding configurations, shown in Figure 2.17.

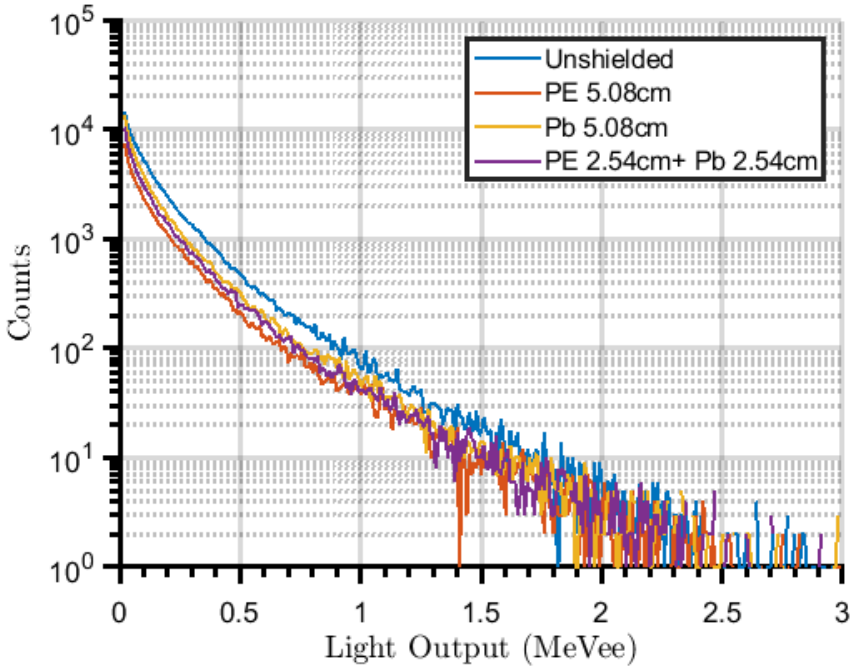

Figure 2.17: Library of MPPost generated light output spectra for each of the MCNPX-PoliMi simulated shielded BeRP ball experiments.

Table 2.2 reports the predicted probability from the unmixing algorithm of material occurrence in the four shielding scenarios. Each input spectrum included 50,000 counts. Poisson noise was added to each mixture to simulate noise due to counting statistics. Each simulated shielding configuration was generated 100 times and the average of the trials was used as input mixture to the algorithm.

Table 2.2: Predicted probability of material occurrence in each of the input analyzed light-output spectra. Row label indicates the material actually present in the simulated shielding configuration.

	PE	**Bare**	**Lead**	**PE & Lead**
PE (5.08 cm)	**0.999**	0.035	0.029	0.027
Bare	0.061	**0.999**	0.047	0.122
Lead (5.08 cm)	0.025	0.028	**0.999**	0.027
PE (2.54 cm) & Lead (2.54 cm)	0.056	0.129	0.089	**0.999**

As indicated by the maximum probability for the correct shielding configuration indicated in Table 2.2, the algorithm is effectively able to distinguish between the different light output spectra with the addition of Poisson

noise. Although this result shows the ability for light output spectra to be distinguished between, having a library composed of many light output spectra possibilities is not very practical for security applications. A library composed of many light output spectra from predetermined shielding configurations may not be possible when trying to determine the identity of the shielding material of a SNM source in a verification scenario. As such, further possibilities for the creation of a generalized library were explored.

2.7.2 Shielding Isotope Mixtures

The primary explored possibility for creating a generalized library is the cross-section-modified neutron energy spectra that is presented in section 2.6. The first step in this methodology was seeing if the algorithm can determine the compositional identity of mixed cross-section-modified neutron energy spectra using a library of the cross-section-modified neutron energy spectra. Common shielding isotopes were chosen, and a simulated bare BeRP ball neutron spectra was modified by each of the isotope's cross section through Equation 2.7. Mixtures of these modified neutron spectra were then created at various numbers of total counts. Unmixing was then performed over 100 Poisson-noise-added iterations and averaged to create the heatmaps shown in Figure 2.18 below that display the predicted presence probabilities of each of the modified spectra:

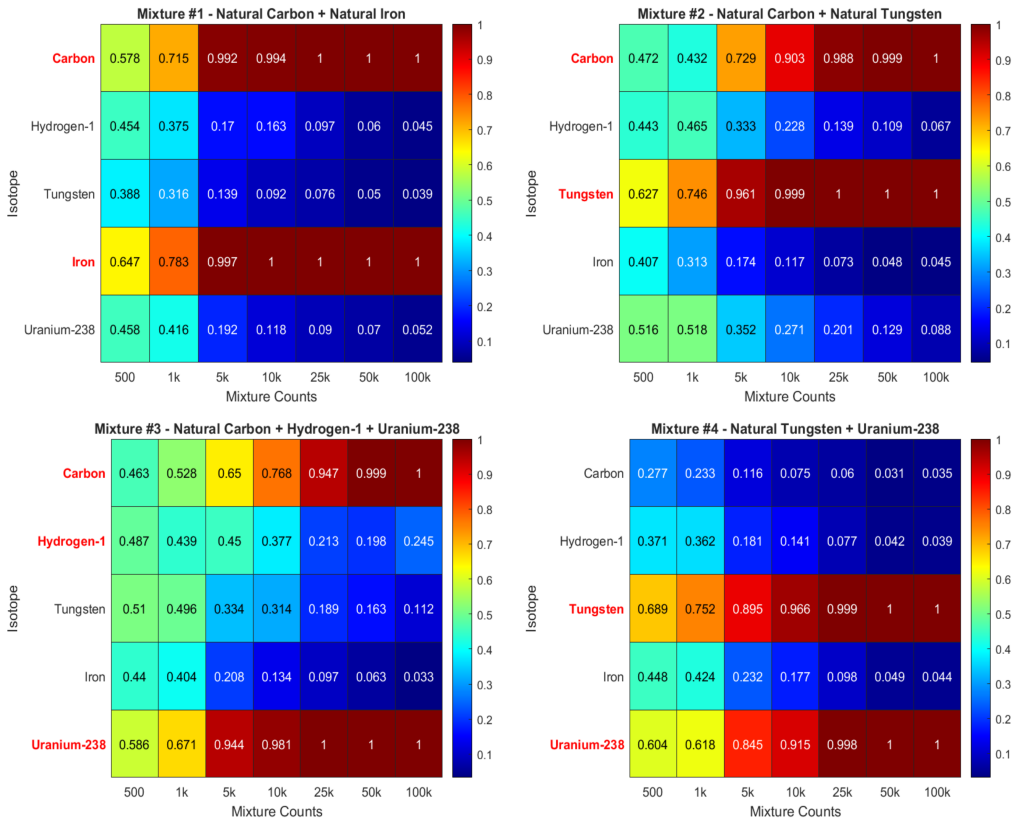

Figure 2.18: Heat maps of four mixtures of different shielding materials with the fixed BeRP Ball neutron source. Materials highlighted in red indicate the present materials in each mixture. A probability of 1, corresponding to 100% certainty or red on the color scale, indicates the algorithm's maximum confidence that this spectra is present in the mixture.

The heatmaps in Figure 2.18 show how with an increasing number of counts, the algorithm becomes more confident in the prediction of the correct modified neutron spectra. Comparing these to gamma radioisotope unmixing scenarios, such as in Figure 2.9, it becomes clear that many more counts are needed to provide an accurate determination for the identity of the isotopes. For reliable identification across any combination of isotopes there needs to be greater than 50,000 mixture counts in the simulated case. However, for the cases where this would applicable, a more time consuming measurement remains feasible for field usage since the sources would be significantly higher activity.

2.7.3 Unfolded Neutron Energy Spectra

The next set of identification testing was performed with the unfolded simulated light output spectra from MPPost, calculated using the methodology outlined in section 2.6.1, to confirm that the algorithm can distinguish between each of the unfolded spectra. This is simply done by testing each of the unfolded spectra as the unknown spectra input to the unmixing algorithm, then using all of the unfolded spectra for each shielding configuration as the inputted library. It is expected that the algorithm would be able to distinguish between them at a low number of counts with high certainty due to the only variation coming from the addition of Poisson noise. Table 2.3 below shows the success of this testing over 100 iterations.

Table 2.3: Unmixing average presence probability results for 100 iterations of comparing the Poisson-noise-randomized unfolded spectra at 5000 counts with a library of all the possible unfolded spectra. The first column indicates the input unknown spectra, while the top row labels represent the algorithm-predicted component.

	Bare	**PE**	**Lead**	**PE & Lead**
Bare	**0.9999**	0.1045	0.1374	0.1391
5.08 cm PE	0.1023	**0.9999**	0.1010	0.1591
5.08 cm Lead	0.1003	0.0793	**0.9999**	0.1269
2.54 cm Each	0.1035	0.1434	0.1639	**0.9999**

With the algorithm being able to distinguish between each of the input unfolded spectra, as indicated by the confirmation of each spectra identity with a 99.99% certainty in 2.3, the final step of testing the viability of the cross-section modified library can be performed.

2.7.4 Unfolded Neutron Energy Spectra with Calculated Spectrum Library

The algorithm is able to identify the differences between spectra of the similar shape of the unfolded shielded spectra, but the cross-section-modified library poses a new challenge since the unknown spectra and the library may have differences outside of only Poisson noise. The calculated spectra are obtained by applying the attenuation law and using a macroscopic cross-section library

(Equation 2.7). Each macroscopic cross-section is composed of an unshielded spectra modified by the cross section of three different isotopes: carbon-12, lead-208, and hydrogen-1. The combination of carbon and hydrogen make up the isotope components of the polyethylene slabs, while lead-208 represents the most prominent lead isotope found in the lead shielding slabs. The library of modified spectra is shown in Figure 2.19.

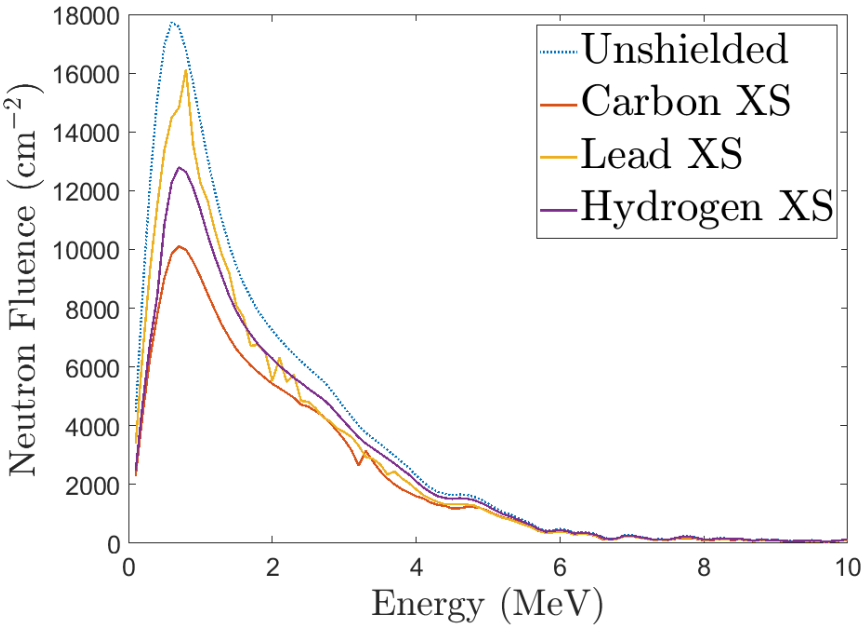

Figure 2.19: Library of the cross-section modified neutron spectra to simulate the effect of 5.08 cm shielding layers placed between the detector and the BeRP ball.

Each of the calculated curves in Figure 2.19 indicates how the spectra has changed as a result of the varying cross section of the shielding material. Comparing Figure 2.19 to Figure 2.15 shows how the spectra shape remains similar between the corresponding cross section to shielding material, with each individual spectra having a comparable scale when compared to the unfolded spectra counterpart. Using this library I was then able to compare the unfolded neutron spectra with this modified cross section library.

In a similar manner to previous tests, the unmixing was performed over 100 iterations of comparing the Poisson-noise-randomized unfolded spectra with the library of cross-section-modified bare BeRP ball spectra. While the unfolded shielded spectra were able to be matched with their respective cross-section-modified calculated spectra with high certainty, the algorithm also incorrectly identifies the presence of another shielding material cross

section in each case. In the unfolded PE case, although the PE is identified as being present with the carbon cross section, the lead cross-section modified spectra is also identified with maximum certainty.

Although the algorithm does predict that the true shielding material is present in higher proportion than the misidentified materials, the high certainty in the misidentification makes this result appear unreliable for predicting the shielding material identity. The similarities shown between the corresponding spectra in Figures 2.15 and 2.19 do not directly correlate to the ability for the algorithm to be able to correctly identify the cross-sectional components. The scaling of each of the spectra when compared to the unshielded case is correct, but the shape of each of the unfolded spectra is being identified as closest to the lead cross-section modified spectra regardless of the scale. Additionally, the shape of the spectra does not change very significantly away from the unshielded spectra, making it prominent in each of the identifications.

Because of these results, the primary methodology remains to use the light output spectra to perform the unmixing of shielded neutron spectra. This method, while successful in providing accurate unmixing results, requires a library that is well developed for many different combinations of shielding materials, such as that shown in Table 2.3. The cross-section modification method only requires that the library consists of cross-section modified SNM spectra, making it more desirable from an operational perspective because the library does not depend on the detector response. The proposed cross-section modification methodology will continue to be developed to allow for unmixing in less ideal scenarios with more accurate identification.

Chapter 3

Diamond-based Betavoltaic Devices

3.1 Background and Methodology

Diamond is highly desirable for our research due to its unique mechanical and electronic properties [32]. The large indirect band gap (5.5 eV) allows for a longer diffusion length for minority carrier collection ($40\mu m^2$), and the high bond strength reduces damage and defects that can reduce minority carrier lifetime. The band-gap is among the largest of any common semiconductor, especially those that are from a single element and indirect; for example, silicon has a band-gap of 1.14 eV and germanium has a band-gap of 0.67 eV. Allowing for collecting electron-hole pairs generated by ionizing radiation without the need to mitigate thermal noise charge carriers through cooling.

Diamond is already well known to be resilient to radiation damage and is applied in radiation detection and shielding. An emerging application of diamond is betavoltaics. These "nuclear batteries" are attractive for niche applications where maintenance on the device is very difficult or impossible such as long-term or extreme environmental monitoring. Nuclear batteries are typically comprised of two elements, the radioactive source and a semiconductor junction that together convert the radiation into a usable voltage. In addition to the attractive electronic and mechanical properties of diamond as the semiconductor in a betavoltaic device, diamond could be grown with carbon-14 (^{14}C) to incorporate the radiation emitter in the semiconductor material. This may theoretically allow for more efficient radiation collection when compared to previous designs.

To find the potential power density of a CVD diamond battery design, a simulation was performed using a layered structure of 20 diamond CVD Schottky junctions, each 20 μm thick, with a 5 μm thickness depletion region. First, we assume a 100% collection efficiency in the depletion region and ignore the effect of charge collection in the surrounding regions. We then

simulated the energy deposition from 156 keV β particles emitted by ^{14}C to be of average energy 49.47 keV. The full structure was considered diamond enriched to 50% weight fraction in ^{14}C, yielding an activity of approximately 20 mCi. This simulation setup is shown in Figure 3.1 below:

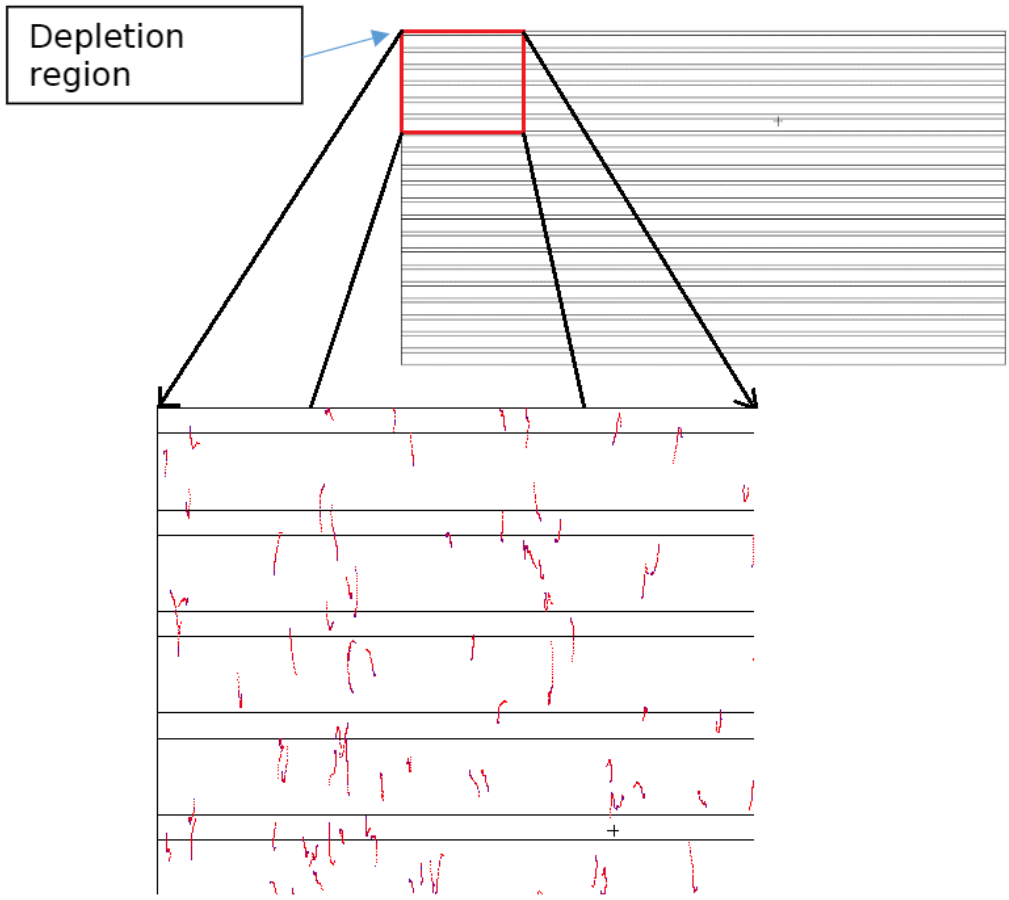

Figure 3.1: Cross section of the simulated battery package, with 20 diamond CVD layers and separating depletion regions. The zoomed-in image displays the simulated electron tracks within the CVD and depletion region layers.

The electron tracks presented in Figure 3.1 represent electrons from ideal ^{14}C in the bulk semiconductor. The color of the particle represents the energy, with high energy represented in red and low energy in blue. Towards the end of each path the interaction points get close together and the energy decreases in agreement with the expected energy loss in the media for electrons. Although the particles are not produced in the depletion region only, and rather by the ^{14}C in the bulk material, many of the tracks terminate in the depletion region and deposit their energy inside, allowing for this energy

to be harvested for use as a battery. The obtained energy deposited was 0.017 MeV per unit β particle, with the range being estimated to be 8.7 μm. With there being 20 diamond CVD layers, each being 20 μm thick, this range is low enough to stop most of the inner particles. Using the assumptions mentioned above, the nuclear radiation generated current I_r can be calculated as in Equation 3.1:

$$I_r = qA\frac{E_{dep}}{\epsilon} \tag{3.1}$$

where q is the electron charge ($1.6{*}10^{-19}$ Coulomb), A is the source activity (1 GBq), E_{dep} is the deposited energy as simulated in MCNP, and ϵ is the energy needed to generate an electron-hole pair (13 eV) [5]. The open circuit voltage is then calculated as in Equation 3.2, assuming that the short-circuit current equals the nuclear radiation generated current:

$$V_{oc} = \frac{kT}{q}ln(\frac{I_r}{I_0} + 1) \tag{3.2}$$

where k is the Boltzmann constant ($1.38 * 10^{-23}\frac{m^2*kg}{s^{-2}K^{-1}}$), T is the absolute temperature in Kelvin (293 K), and I_0 is the leakage current of 50 pA (guess based on [5]). The maximum power output can then be calculated as in Equation 3.3 and assuming a unit fill factor:

$$P = V_{oc} \times I_r \tag{3.3}$$

This results in an estimated power density of 12 $\mu W/cm^3$, which is comparable with recently developed nuclear CVD diamond batteries based on ^{63}Ni decay [5]. Thus, this technology would allow for usage in low-power applications in harsh environments where battery replacement is not practical.

In general, plasma-enhanced chemical vapor deposition is a well-established approach to growing diamond. Diamond, as opposed to graphite or amorphous carbon, is obtained by controlling the gas mixture. Typically, gas mixtures of methane (CH_4) and hydrogen (H_2) are used, with mostly hydrogen, e.g., 99:1 H_2:CH_4 [17]. To obtain ^{14}C containing diamond, we propose that

^{14}C containing CH_4 could be introduced in the gas mixture. The amount of ^{14}C or ^{14}C containing CH_4 would control the amount of ^{14}C that ultimately ends up in the diamond films.

Many different types of reactors and plasmas have been studied for diamond growth. Here, we focused on a remote radio-frequency-powered plasma system which has the advantage of providing the necessary radicals for diamond nucleation and growth, while minimizing ion bombardment which could lead to defects. The design and building of this chamber are the main focuses of this chapter as many design considerations were needed to produce diamond. Additionally, a simulation in COMSOL was developed to assess the heat dissipation from the substrate heating that is required to grow diamond films.

3.2 Plasma Reactor Design

Our initial design for the plasma reactor was a stainless steel cube with six 2.75" Conflat flanges. The flanges allow entry points for the various components of the reactor including the vacuum pumping, substrate holder, pressure gauges, and the remote plasma. We decided on a heated substrate which would localize the high temperature to near the substrate. Nonetheless, at the high temperatures that are needed for diamond growth (> 800°C) there is still enough heat and heat dissipation for the reactor walls to become hot. In particular, our chamber contains a viewport window, which contains a seal that cannot go above $\sim$300°C.

3.2.1 COMSOL Simulation

In order to assess the heat dissipation in our reactor, a COMSOL simulation was developed. COMSOL allows for the customization of many different physics modules to incorporate in the model and utilizes an adjustable finite element method to determine different properties along the chamber geometry. The main source of heating is radiation from the substrate heater. Because the substrate must be heated to 800–1000°C in order for diamond to be grown, the chamber walls will be receiving a large amount of radiating energy from this heating element. The main source of cooling is the input gas flow which removes heat through convection. The degree to which the

heat source and gas cooling will impact the wall temperature becomes an important aspect that will be monitored in both this simulation and in the physical chamber once operational.

The design of the simulated chamber follows as closely to the intended physical chamber as possible, using exact dimensions of the many different components. The layout of this design is shown in Figure 3.2 below:

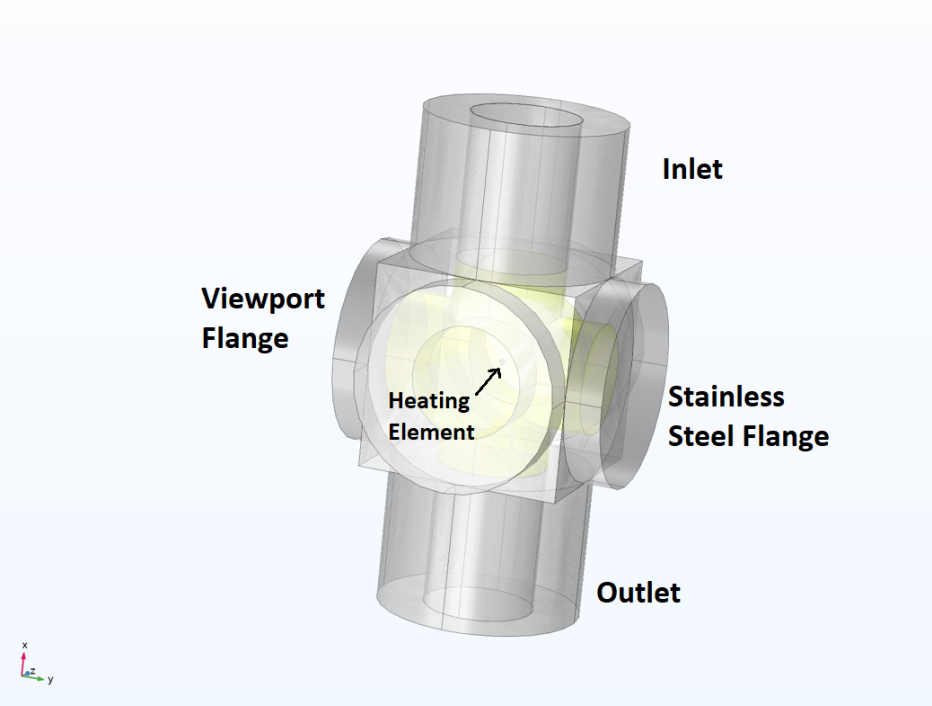

Figure 3.2: Layout of the COMSOL simulation geometry matching the design of the physical chamber once fully assembled.

As shown in Figure 3.2, the reactor consists of a cube with flanges on four of the sides and two inlet and outlet pipelines. On one side, the flange material is glass to match the viewport window that will be used to look into the chamber. Three of the other sides consist of 2.75" stainless-steel flanges that are sealed with a copper gasket. The final two pipeline sides are 2.75" stainless-steel extensions that are attached to the chamber in the same way as the flanges with the copper gasket. The upper inlet pipeline produces a laminar flow of (H_2) gas into the chamber at a rate of 50 mL/s, where a flow physics module allows for the gas to flow seamlessly through the chamber and out the outlet pipeline. In the central chamber lies the substrate heater which is set to 1000 °C and uses many heat transfer modules to achieve the most realistic simulation. The outside of the chamber is surrounded completely by

air which assists in cooling down the chamber with the convection physics module. These physics elements combined should allow for this simulation to match as close to the physical scenario as possible.

The testing of this simulation becomes simple once this geometry is set up, with a few minor parameters that need to be set up. The simulation was set to run for 10,000 seconds to go beyond the deposition time for a thin diamond film. Additionally, all of the other physics modules including convective and conductive heat transfer, surface-to-surface radiation, and laminar flow for the gas moving through the chamber were initialized for the geometry. After 10,000 seconds of simulation, the heat plots shown in Figures 3.3 and 3.4 below were obtained:

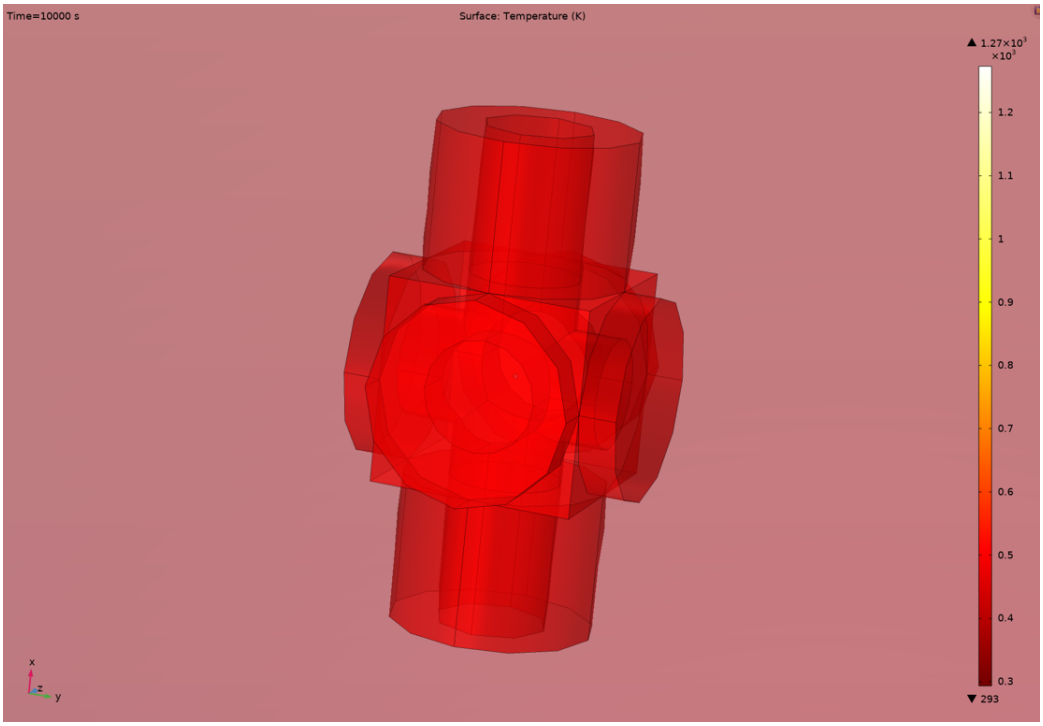

Figure 3.3: Heat plot showing the temperature of the simulated geometry after 10000 seconds of running with all relevant physics modules enabled.

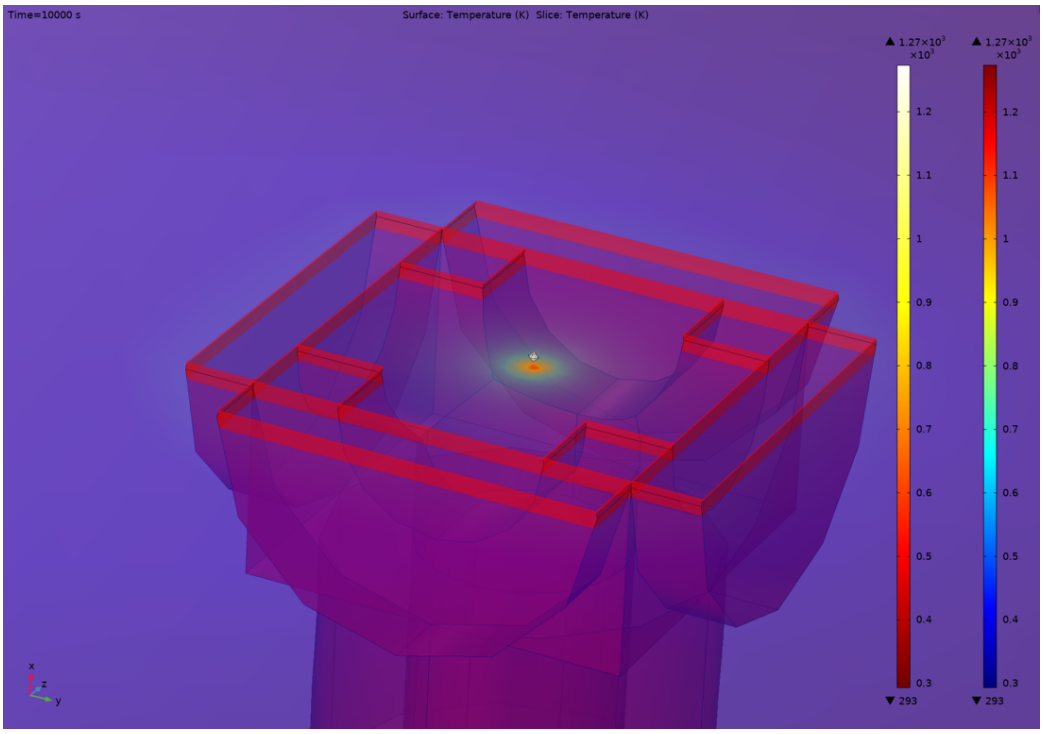

Figure 3.4: Cross section of the heat plot through the center of the chamber showing the heating element and inner wall temperature distribution.

Figures 3.3 and 3.4 show how the temperature of the chamber walls increase greatly over the course of the simulation to about 440 K after 10000 seconds. The cross section image in Figure 3.4 shows how the heating element radiates heat outward isotropically towards the walls, where they are then heated up over the course of the simulation. The large region of air on the outside of the chamber helps to alleviate the increasing wall temperature with its natural convective properties, allowing for the wall temperature to not increase too quickly beyond the temperature restrictions of the flange seals. A plot showing how the temperature changes over time can be seen in Figure 3.5 below:

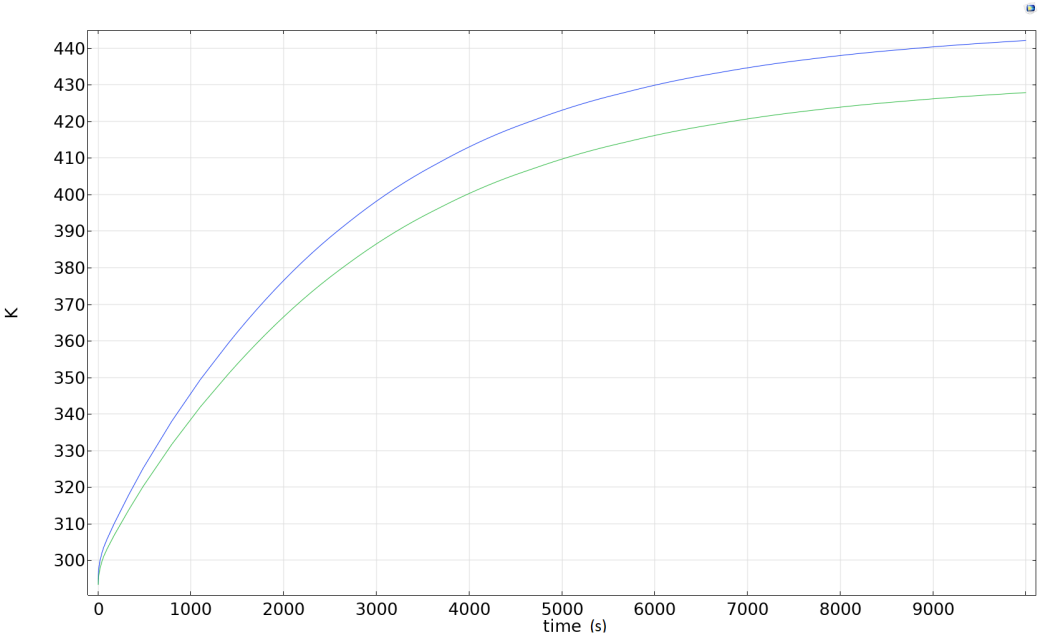

Figure 3.5: Temperature (in Kelvin) change with time of reactor obtained by COMSOL simulation. The blue line corresponds to temperature of the outer wall of the chamber that is touching the flange, whereas the red line represents the temperature 0.5 cm from the outside the chamber in the ambient air.

As shown on Figure 3.5, the temperature increases at a greater rate in the beginning half of the simulation timeline when compared to the latter half. This expected behavior is a result of the temperature gradient between the heating element and the surrounding walls reducing as the temperature of the walls increase. As the red line indicates, the air just outside of the outer walls also will increase greatly in temperature. Although the wall and air temperature will increase to about 120–140 °C, the maximum temperature never exceeds 300 °C, which is the tolerance of the vacuum seals. As such, this temperature allows for the chamber to operate for multiple hours without the risk of losing the vacuum seal or damaging any of the chamber components. However, for longer deposition times where a thicker film is needed, outside cooling of the chamber from a fan would likely be required as the temperature would continue to increase, although at a reducing rate, when going beyond this simulation time frame. This simulation effectively assisted in confirming the viability of this design.

3.2.2 Plasma Reactor Setup

With the simulation showing promising temperature profile results, I was able to proceed with designing the chamber to house the substrate and plasma for diamond deposition. The chamber design can be split into four essential stages and regions: 1) gas inlet flow, 2) remote plasma, 3) central chamber and substrate, and 4) vacuum pumping.

The gas inlet flow is controlled by digital mass flow controllers (MFCs) that set the flow rate of gases from gas cylinders. In our case, the gases flow through the plasma and then towards the substrate. Two total MFCs are used in this plasma reactor, one for each gas, CH_4 and H_2.

The remote plasma consists of a quartz glass tube with a ring electrode powered by a RF (13.56 MHz) power supply. The bulk of the complexity in this region comes from the creation a matching box between the power supply and the electrode. The matching box consists of variable inductors and capacitors that can be tuned to match the impedance of the RF transmitter and receiver signal. The details of building this component are outlined in the chamber construction section below. When used in combination with the RF power supply, this allows for a stable plasma to form inside of the quartz tubing that will extend into the central chamber. This quartz tube is connected via a sealing Ultratorr adapter to the top flange of the cubic chamber, allowing for the plasma to assist in the diamond chemical vapor deposition process as it comes into contact with the substrate.

The central chamber region consists of six flange sides that each will allow for a different component to have access to the central region of the chamber where the substrate will be held. The different components that will be used are: the quartz tube where the remote plasma is generated, a viewport, substrate holder and heater, pressure sensing, and a vacuum line. A final port can be used for any further applications that may be needed in future experiments, and for now can be sealed with a blank 2.75" flange. The substrate holder and heater components will be an extension that is placed on the chamber, allowing for a substrate to be inserted onto the holder and more easily removed for testing. Additionally, a thermocouple will need to be inserted from this side to confirm that the temperature of the substrate remains high enough for proper diamond depositon. The pressure sensing side will be performed using a Baratron pressure gauge that will confirm

that the chamber remains under the expected pressure conditions. Lastly, the vacuum output will utilize the bottom flange to pressurize the chamber and act as an outlet for the gas flow through the central chamber. The central chamber without any attachments is shown in Figure 3.6 below:

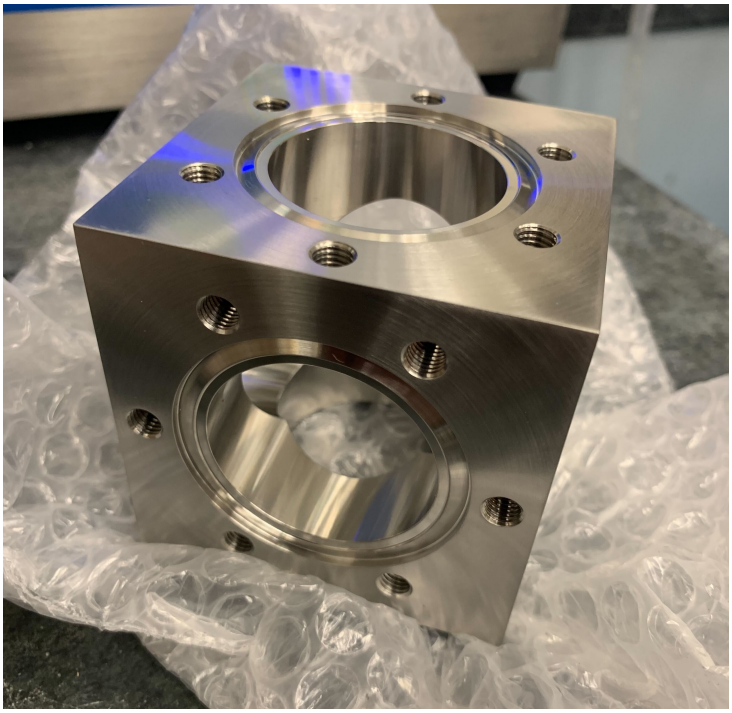

Figure 3.6: The stainless-steel 2.75" cubic chamber without any attachments. Each side will be used for a different component, with the plasma reaching the center of the chamber where the substrate holder will be placed.

The vacuum outlet consists of the outlet tubing connecting the chamber to the vacuum pump, a convectron pressure gauge, a valve for controlling the pumping down of the chamber, and the vacuum pump. The pressure gauge used in this section is placed on the opposite side of the valve so that it can be compared with the pressure inside the chamber. The vacuum pump used an oil mist eliminator on the outlet to trap any oil that may have been remaining in the gas before being sent out for disposal. The inlet side of the pump used an inlet trap that restricts any possible debris that may have escaped out of the chamber and stops it from possibly damaging the pump machinery. When running, this pump allows for the base chamber pressure to reach about 15 mTorr. When fully assembled, this chamber will be secured on top of a tall stand that allows for the vacuum pump to be placed underneath. This allows for minimal space usage while also achieving

plasma formation in a relatively small chamber.

3.2.3 Plasma Reactor Construction

The construction of the plasma chamber was split into several stages, beginning with the building of the stand, then the chamber and its attachments, and lastly the design and building of the matching box. The stand was designed to allow for the bottom port of the chamber to fit through an aluminum plate and allow for the hose to reach the vacuum pump input. The chamber can then be held via a series of stabilizing brackets and allow for any attachments to extend across the aluminum plate as needed. The stand was designed to be a movable workstation that can be adapted to the lab space as needed without the need for taking apart many parts of the chamber. Figure 3.7 below shows this stand prior to the mounting of the chamber:

Figure 3.7: Custom built movable stand for holding and stabilizing the cubic plasma chamber. The aluminum plate mounted on top was machined to have an output hole to go towards the vacuum pump underneath.

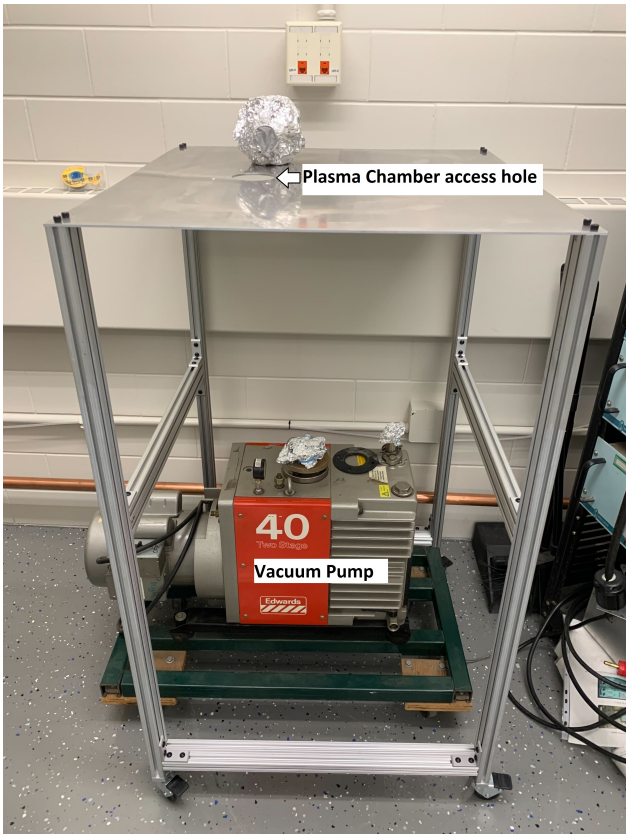

Figure 3.8: Stand with vacuum pump in place underneath the stand for ease of access to the chamber.

The space underneath the higher-up horizontal bars in Figure 3.7 allow for the vacuum pump, which is similarly movable with mounted wheels, to be slid in for maximization of lab space. An image with the pump in place is shown in Figure 3.8 as well. The vacuum inlet for the pump can then be directly placed underneath the chamber, allowing for easy access to the chamber components underneath the aluminum plate.

The next component that required building and testing was the plasma chamber and its necessary attachments. Each side was chosen for a different purpose and parts were attached to each side to better fit these needs. For each attached flange a copper gasket was placed in between the chamber and the flange to provide an air-tight seal necessary for the vacuum pressure. The bottom port of the chamber was equipped with a conical reducer that heads towards the valve, pressure gauge, and vacuum pump. One of the horizontal sides uses a viewport flange to allow us to see into the chamber to ensure that the plasma is reaching the substrate. Another horizontal side was built to

utilize a Baratron pressure gauge by adapting to a smaller conflat flange size that was needed for attachment. The final used side will house the substrate heating element and the substrate holder as well as any sensing equipment through the use of a longer extension arm attached to the central chamber. The final attachment uses the top port of the chamber, where the plasma will be entering in through an Ultratorr adapter connecting to a quartz glass tube. A diagram of the partially assembled chamber and on the stand are shown in Figure 3.9 below:

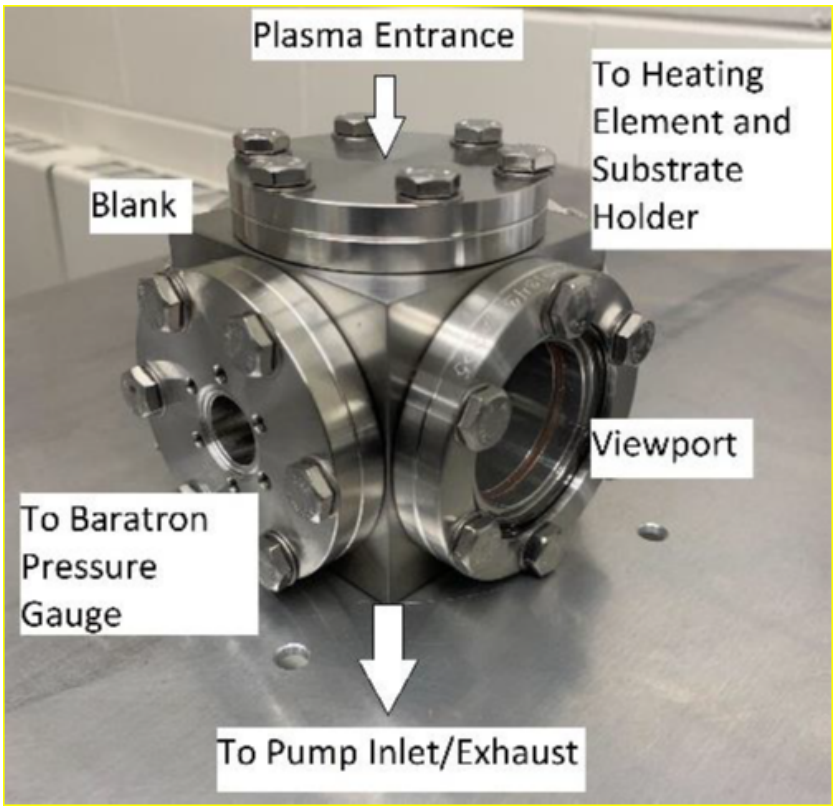

(a) Partially assembled chamber with attached flanges on the aluminum plate. The labels indicate the purpose of each side or the part that will be attached for the deposition process.

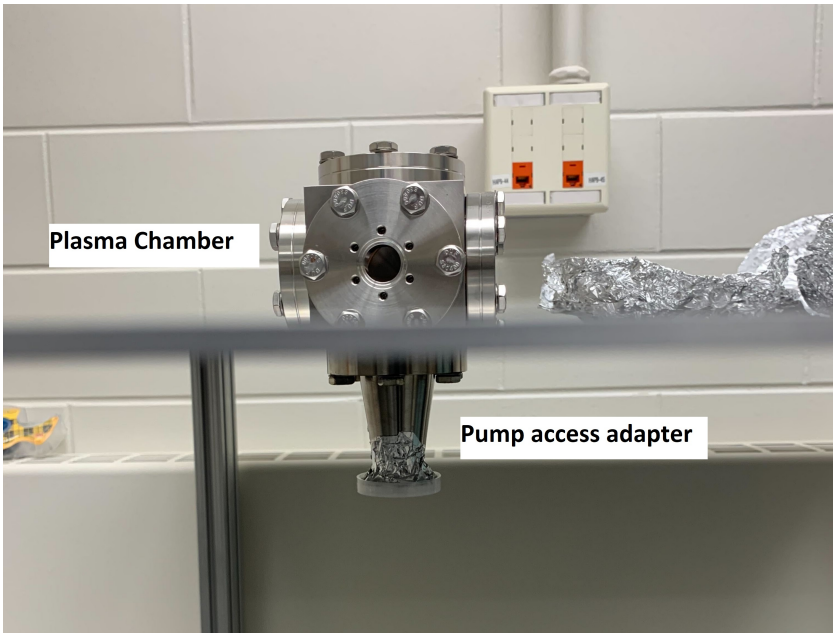

(b) Side view of the chamber placed on the aluminum plate to show the bottom port going through to be attached to the vacuum pump.

Figure 3.9: Partially Assembled cubic plasma chamber with attachments shown from different angles for better visualization.

Before many of the other attachments were added to the chamber, a test on the ability to pump down the chamber was needed to ensure that the chamber is fully sealed. Performing this test now and with each large addition to the chamber makes finding any possible leaks significantly easier. As such, the Baratron pressure gauge flange was sealed and a gauge was attached to the bottom conical reducer, along with a hose going to the vacuum pump inlet. The pump was then run for about 5 minutes to check if the chamber was holding a vacuum pressure with no leakage. An image of this testing setup is shown in Figure 3.10 below:

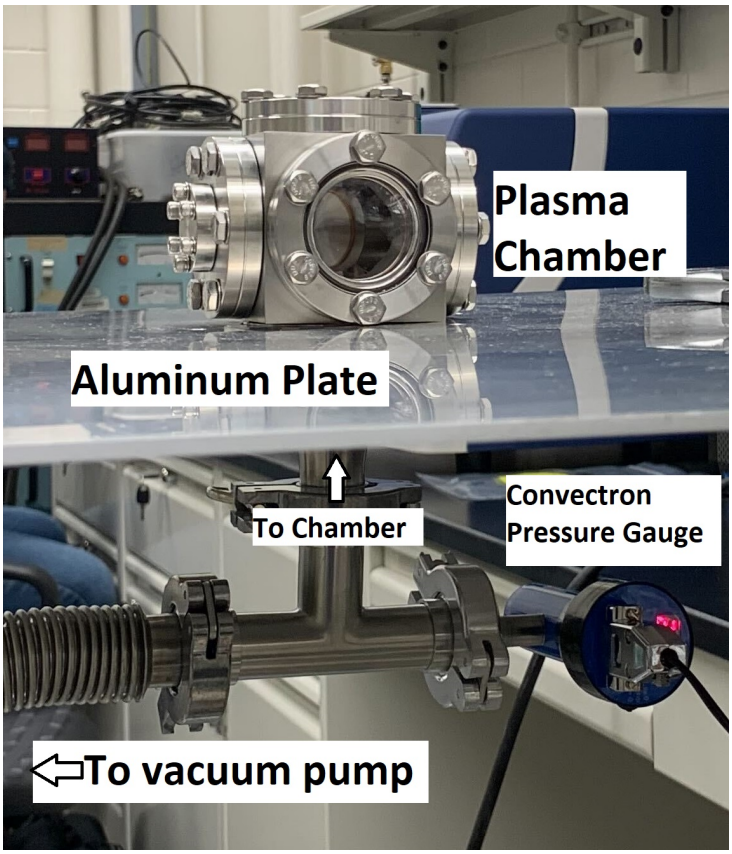

Figure 3.10: Testing setup for pumping down the chamber to check for leaks and pressure retention.

Performing this test with the vacuum pump both confirmed that the chamber could hold the vacuum pressure, as well as the pump's ability to lower the vacuum pressure to that needed for diamond deposition. With this aspect of the design tested, along with confirming that the pump allows for the experimental parameters to be met, many of the other components can then be attached to the plasma chamber. The next part to construct is the

plasma formation region within the quartz glass tube. While this is driven primarily by the input gasses and the RF power supply, the matching box for the RF signal needs to be constructed as well. The matching box is used to match impedance between a transmitter and receiver signal through means of manually adjusting the capacitance and inductance of two variable capacitors and a single variable inductor in a circuit. The circuit diagram for the matching box is shown in Figure 3.11 below:

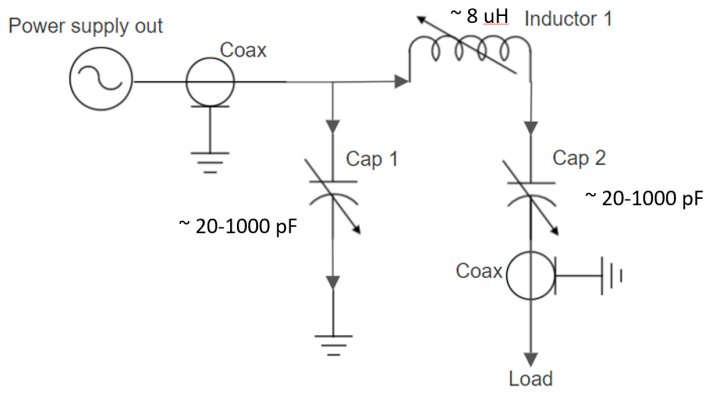

Figure 3.11: Circuit diagram for the matching box, including the approximate ranges for the inductor and capacitors.

The circuit diagram in Figure 3.12 shows how this circuit can be created to achieve the impedance matching using the input RF power supply signal. Using this proposed circuit, a custom matching box was built using a series of variable capacitors and an inductor inside an aluminum box housing. The variable capacitors were variable air core capacitors from Oren Elliot Products, and the variable roller inductor was from RF Parts Company. These primary components were then placed into the aluminum box housing with ceramic standoffs to separate the components from the ground. Each of these components has a central rod that can be turned to adjust the capacitance or inductance of the component. These rods, when extended to outside of the box, are then attached to marked plastic knobs that allow for adjustment of the RF signal matching while in use. This aluminum box was assembled as shown in Figure 3.12 below:

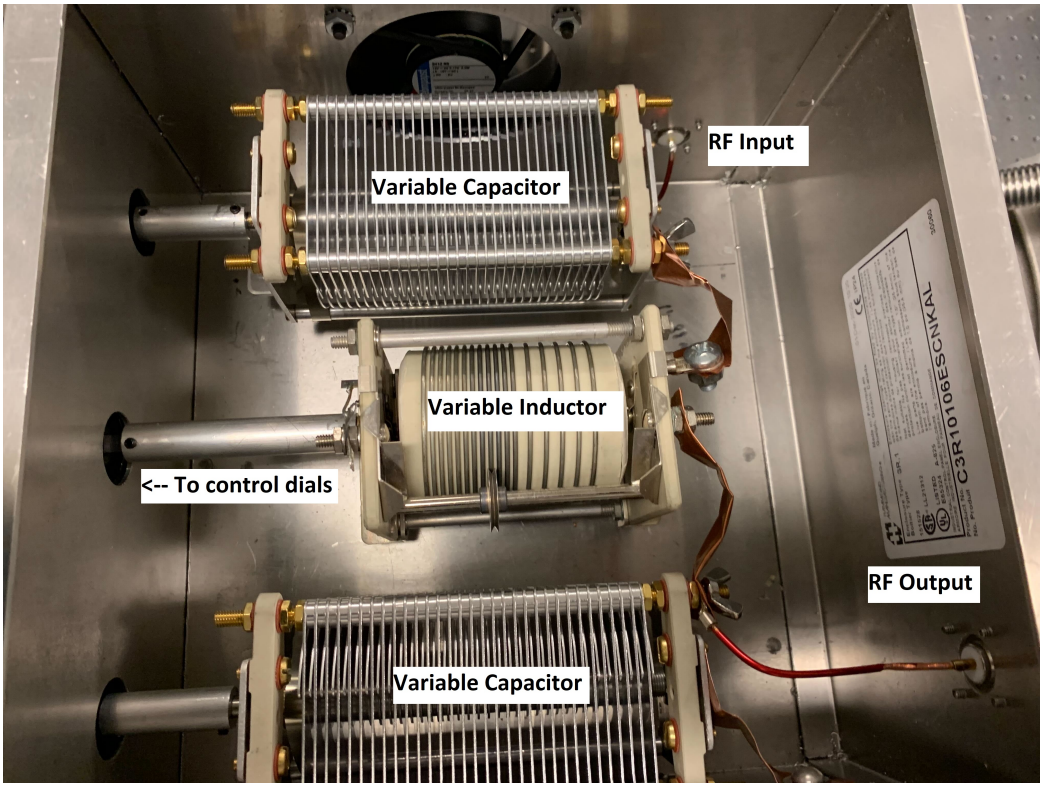

Figure 3.12: Fully Assembled matching box with connections for input RF signal and output RF signal. The middle component is the variable inductor, while the two outside components are the variable air core capacitors.

Additionally, Figure 3.12 shows a fan cutout on the far side of the box, allowing for cool air to flow into the box and keep any components from overheating. Attaching the RF input power to this box and routing the output RF signal to the electrode on the plasma formation region on the chamber setup will allow for a plasma to form once the capacitance and inductance are properly adjusted using the dials. The construction of this matching box and testing to ensure that it works to create a plasma finalizes the equipment building that is needed before a plasma can be tested with the chamber.

3.3 Future Work

This project requires many steps to achieve the end goal of consistently producing a diamond thin film that can be usable for radiation detection purposes. With the chamber built, simulated, and many of the components tested and built individually, performing the deposition process remains the

next goal for this project. A calibrated MFC power supply and the attachment of the quartz glass tube and electrode are the final remaining components needed before a plasma can effectively be created and tested in the chamber. Once a plasma is tested and successfully run using our predetermined parameters, the substrate heater and the substrate holder arm can be attached to achieve diamond deposition. These components require an additional extension to be added onto the previously blank flange of the chamber where substrates can be more easily inserted and removed. Once a substrate can be heated and inserted into the system, then material deposition can be carried out. Using both Raman spectroscopy and electron microscopy, the structure of the diamond film can be analyzed and changes can be made to the deposition process. One of the main attributes that must be checked is the presence of graphite or any other defects that may have formed during the deposition. Checking on the structure of the crystal formation can also determine if the deposited diamond is single-crystalline or poly-crystalline, which may have an effect on the detection capabilities of the diamond. As such, these further steps will be taken to advance and improve upon the plasma reactor setup and grown materials.

Chapter 4

Conclusions

This work details the process for using the unmixing algorithm to identify both a neutron source and its shielding material. Spectra data was acquired of the BeRP ball at the Device Assembly Facility using a deuterated trans-stilbene scintillation detector that was shielded by a variety of material types and combinations. These setups were recreated in MCNPX-Polimi in order to have a simulated data set to compare the measured data against. The processing of the data has included a few main steps: pulse-shape discrimination, unfolding, and unmixing. The process for pulse-shape discrimination is able to distinguish between neutron and gamma pulses based on the comparable size between the pulse tail area and the pulse total area. Additionally, this algorithm uses a pile-up rejection methodology that looks for secondary peaks and is able to classify the peaks as rejected if the secondary peak is beyond a set threshold. Once the optimal PSD parameters were chosen and the neutron pulses could be effectively separated from the gamma pulses, a detector characterization study was performed to find the response matrix created by the detection of 0.1 to 20 MeV incident neutrons. Creating this response matrix allows for the unfolding of the neutron light output spectra of the DAF measurements to find the neutron energy spectra incident on the detector. This is performed by using the response matrix over many iterations to estimate how the neutron spectra would be based on the shielded light output spectra. These neutron energy spectra can then be compared with a library of simulated cross-section modified BeRP ball spectra using the unmixing algorithm to see if the shielding material can be identified correctly. The success of this method allows for further expansion of the unmixing library to more shielding materials and use of the algorithm on special nuclear material measurements.

This work also demonstrates the building of a plasma vacuum chamber for use in a diamond chemical vapor deposition setup. Building a chamber that

is able to effectively deposit diamond films onto a substrate would allow for many useful applications such as diamond detection devices and diamond-based betavoltaic cells. The design of this chamber uses a compact, 2.75" cubic chamber that can use each side port for a different purpose or device. The top port is used for a plasma tube, in which a RF plasma will be stabilized and will assist with the deposition process. The side ports are used for various tools and devices that will help to regulate the deposition process, such as a pressure gauge, the substrate holder and heater, and a viewport. The bottom port provides the flow-through point for the gas entering the chamber as it heads through a hose to the vacuum pump for pressurizing the chamber. This setup was simulated using COMSOL to confirm the designs viability and to ensure that the temperature would not go beyond the seal threshold of 300 °C. Lastly, a matching box was designed and constructed to assist in the stabilization of the RF plasma. With this chamber built and the surrounding components tested, the plasma chamber is prepared for the first rounds of plasma stabilization testing and creating a diamond film. When the diamond films are created and analyzed, the final goals of our current work will be to create many-layer beta-emitting films for betavoltaic cell applications, along with the production of diamond films for radiation detection applications.

Chapter 5

References

[1] D.T. Connor, P.G. Martin, H. Pullin, K.R. Hallam, O.D. Payton, Y. Yamashiki, N.T. Smith, and T.B. Scott. Radiological comparison of a fd-npp waste storage site during and after construction. *Environmental Pollution*, 243:582–590, 2018.

[2] David L. Chichester and Edward H. Seabury. Using electronic neutron generators in active interrogation to detect shielded fissionable material. In *2008 IEEE Nuclear Science Symposium Conference Record*, pages 3361–3367, 2008.

[3] S Salaymeh and R Jeffcoat. Radioisotope identification of shielded and masked snm rdd materials. 2010.

[4] M. Weiss, M. Fang, Y. Altmann, M.G. Paff, and A. Di Fulvio. Effect of natural gamma background radiation on portal monitor radioisotope unmixing. *Nuclear Instruments and Methods in Physics Research Section A: Accelerators, Spectrometers, Detectors and Associated Equipment*, 1002:165269, 2021.

[5] V.S. Bormashov, S.Yu. Troschiev, S.A. Tarelkin, A.P. Volkov, D.V. Teteruk, A.V. Golovanov, M.S. Kuznetsov, N.V. Kornilov, S.A. Terentiev, and V.D. Blank. High power density nuclear battery prototype based on diamond schottky diodes. *Diamond and Related Materials*, 84:41–47, 2018.

[6] C. Delfaure, M. Pomorski, J. de Sanoit, P. Bergonzo, and S. Saada. Single crystal cvd diamond membranes for betavoltaic cells. *Applied Physics Letters*, 108(25):252105, 2016.

[7] T. Shimaoka, H. Umezawa, K. Ichikawa, J. Pernot, and S. Koizumi. Ultrahigh conversion efficiency of betavoltaic cell using diamond pn junction. *Applied Physics Letters*, 117(10):103902, 2020.

[8] P. Bergonzo, A. Brambilla, D. Tromson, C. Mer, B. Guizard, F. Foulon, and V. Amosov. Cvd diamond for radiation detection devices. *Diamond and Related Materials*, 10(3):631–638, 2001. 11th European Conference on Diamond, Diamond-like Materials, Carbon Nanotubes, Nitrides and Silicon Carbide.

[9] P Bergonzo, D Tromson, and C Mer. Radiation detection devices made from CVD diamond. *Semiconductor Science and Technology*, 18(3):S105–S112, feb 2003.

[10] T. Shimaoka, S. Koizumi, J. H., and Kaneko. Recent progress in diamond radiation detectors. *Functional Diamond*, 1(1):205–220, 2021.

[11] John K. Mattingly. Polyethylene-reflected plutonium metal sphere : subcritical neutron and gamma measurements. 11 2009.

[12] J. Zhou, N. Gaughan, F.D. Becchetti, R.O. Torres-Isea, M. Febbraro, N. Zaitseva, and A. Di Fulvio. Light output quenching in response to deuterium-ions and alpha particles and pulse shape discrimination in deuterated trans-stilbene. *Nuclear Instruments and Methods in Physics Research Section A: Accelerators, Spectrometers, Detectors and Associated Equipment*, 1027:166287, 2022.

[13] N. Gaughan, J. Zhou, F.D. Becchetti, R.O. Torres-Isea, M. Febbraro, N. Zaitseva, Y. Altmann, and A. Di Fulvio. Characterization of stilbene-d12 for neutron spectroscopy without time of flight. *Nuclear Instruments and Methods in Physics Research Section A: Accelerators, Spectrometers, Detectors and Associated Equipment*, 1018:165822, 2021.

[14] Horst Klein and Frank Brooks. Scintillation detectors for fast neutrons. page 097, 01 2007.

[15] P. W. May, J. N. Harvey, J. A. Smith, and Yu. A. Mankelevich. Reevaluation of the mechanism for ultrananocrystalline diamond deposition from ar/ch4/h2 gas mixtures. *Journal of Applied Physics*, 99(10):104907, 2006.

[16] C. Johnston, C. Ayres, and P. Chalker. EVALUATING THE INFLUENCE OF GROWTH PARAMETERS ON CVD DIAMOND DEPOSITION USING FACTORIAL ANALYSIS. *Journal de Physique IV Proceedings*, 02(C2):C2–915–C2–921, 1991.

[17] D. G. Goodwin. Scaling laws for diamond chemical-vapor deposition. i. diamond surface chemistry. *Journal of Applied Physics*, 74(11):6888–6894, 1993.

[18] F. D. Becchetti, R. O. Torres-Isea, A. Di Fulvio, S. A. Pozzi, J. Nattress, I. Jovanovic, M. Febbraro, N. Zaitseva, and L. Carman. Deuterated stilbene (stilbene-d12): An improved detector for fast neutrons. *Nuclear Instruments and Methods in Physics Research, Section A: Accelerators, Spectrometers, Detectors and Associated Equipment*, 908:376–382, 2018.

[19] M. L. Carman, A. M. Glenn, A. N. Mabe, F. D. Becchetti, S. A. Payne, and N. P. Zaitseva. Solution growth of a deuterated trans-stilbene crystal for fast neutron detection. *Journal of Crystal Growth*, 498:51–55, 2018.

[20] J. Hutchinson. Subcritical measurements of a reflected plutonium sphere using noise techniques. pages 153–159, 2009.

[21] M. Fang, N. Bartholomew, and A. Di Fulvio. Positron annihilation lifetime spectroscopy using fast scintillators and digital electronics. *Nuclear Instruments and Methods in Physics Research, Section A: Accelerators, Spectrometers, Detectors and Associated Equipment*, 943, 2019.

[22] Lukasz Swiderski, Marek Moszynski, Wiesław Czarnacki, Joanna Iwanowska, Agnieszka Syntfeld-Każuch, Tomasz Szczęśniak, Guntram Pausch, Cristina Plettner, and Katja Roemer. Measurement of compton edge position in low-z scintillators. *Radiation Measurements*, 45:605–607, 03 2010.

[23] J.K. Polack, M. Flaska, A. Enqvist, C.S. Sosa, C.C. Lawrence, and S.A. Pozzi. An algorithm for charge-integration, pulse-shape discrimination and estimation of neutron/photon misclassification in organic scintillators. *Nuclear Instruments and Methods in Physics Research, Section A: Accelerators, Spectrometers, Detectors and Associated Equipment*, 795:253 – 267, 2015.

[24] Glenn F. Knoll. *Radiation Detection and Measurement*. John Wiley & Sons, Inc., Hoboken, New Jersey, 2010.

[25] O. Chamberlain, G. W. Farwell, and E. Segrè. ${}_{94}\mathrm{Pu}^{240}$ and its spontaneous fission. *Phys. Rev.*, 94:156–156, Apr 1954.

[26] M. Paff, A. Di Fulvio, Y. Altmann, S. D. Clarke, A. O. Hero, and S. A. Pozzi. Identification of mixed sources with an organic scintillator-based radiation portal monitor. *Journal of Nuclear Materials Management*, 46(4):48–57, 2018.

[27] Expectation-propagation for weak radionuclide identification at radiation portal monitors. *Scientific Reports*, 2020.

[28] T. P. Minka. Expectation propagation for approximate bayesian inference. In *Proceedings of the Seventeenth conference on Uncertainty in artificial intelligence*, pages 362–369. Morgan Kaufmann Publishers Inc., 2001.

[29] Aki Vehtari, Andrew Gelman, Tuomas Sivula, Pasi Jylänki, Dustin Tran, Swupnil Sahai, Paul Blomstedt, John P. Cunningham, David Schiminovich, and Christian Robert. Expectation propagation as a way of life: A framework for bayesian inference on partitioned data, 2014.

[30] Yoann Altmann. Sparse Unmixing Poisson Noise EP.

[31] Haonan Zhu, Yoann Altmann, Angela Di Fulvio, Stephen McLaughlin, Sara Pozzi, and Alfred Hero. A hierarchical bayesian approach to neutron spectrum unfolding with organic scintillators. *IEEE Transactions on Nuclear Science*, 66(10):2265–2274, 2019.

[32] James E. Butler, Richard L. Woodin, Lawrence Michael Brown, P. Fallon, A. H. Lettington, and John Wickham Steeds. Thin film diamond growth mechanisms. *Philosophical Transactions of the Royal Society of London. Series A: Physical and Engineering Sciences*, 342(1664):209–224, 1993.

Appendix A

MCNP Code

A.1 MCNPX-Polimi Input File: 5.08 cm Lead Shielded BeRP ball

```
Shielded BeRP ball simulation
100 6 -1.24    -10         IMP:N,P=1
102 82 -11.35   -12         IMP:N,P=1
200 239 -19.604  -20       IMP:N,P=1
201 240 -8.0     21 -22    IMP:N,P=1
300 7 -2.6989     -30      IMP:N,P=1
301 7 -2.6989     -31      IMP:N,P=1
302 10 -2.3       -32      IMP:N,P=1
900 9 -0.001205   -99 #100 #102 #200 #201 #300 #301 #302 IMP:N,P=1
901 9 -0.001205    99     IMP:N,P=0

c ***********************************************
c
c Surfaces
c
c ***********************************************
c 10   RPP   0 5.08 -2.54 2.54 -2.54 2.54
10   HEX 0 0 0  5.35 0 0  0 3.175 0
12   RPP   -9.08 -4 -15.24 15.24 -15.24 15.24
20   S   -100 0 0 3.7938
21   S   -100 0 0 3.8278
22   S   -100 0 0 3.8583
30   RPP   -120 -80 -16.25 -15.25 -30.48 30.48
31   RPP   -10 30 -16.25 -15.25 -30.48 30.48
```

```
32   RPP   -200 200 -150 -90 -200 200
99   S     0 0 0 500

MODE N P
NPS 2e7
PHYS:N J 20
PHYS:P 0 1 1
CUT:P 2J 0
SDEF POS=-100 0 0 CEL=200 RAD=d1 TME=d2
SP1 -21 2
SI1 0 3.7938
SC2 BeRP ball activity 8.8e5 neutrons/seconds.
SI2 0 2.2727e6
SP2 0 1
IPOL 3 1 2 1 J 1 1 100
RPOL 0.001 0.001
PRINT 10 40 50 100 110 126 140 160
c ************************************************
c
c Materials
c
c ************************************************
c  Deuterated trans-stilbene density = 1.24
M6   NLIB=80c  PLIB=04p
     1001      -0.00063
     1002      -0.12492
     6000      -0.87445
c Lead density = 11.35
M82  NLIB=80c  PLIB=04p
     82000     -1.000000
c BeRP ball cladding - stainless steel 304 density = 8.0
M240 NLIB=80c PLIB=04p
     6000  -0.000400
     14000 -0.005000
     15031 -0.000230
     16000 -0.000150
```

```
     24000 -0.190000
     25055 -0.010000
     26000 -0.701730
     28000 -0.092500
c BeRP ball plutonium compositon density = 19.604
M239 NLIB=80c PLIB=04p
     94238 -0.00016
     94239 -0.93557
     94240 -0.05907
     94241 -0.00068
     94242 -0.00028
     95241 -0.00247
     31000 -0.00034
     6000  -0.00023
     92235 -0.00075
     92236 -0.00017
     40000 -0.00010
     93237 -0.00008
     11000 -0.00005
     92234 -0.00004
     26000 -0.00001
c Aluminum (table) density = 2.6989
M7  NLIB=80c PLIB=04p
     13027    -1.000000
c Air density = 0.001205
M9    NLIB=80c PLIB=04p
      7014  -0.755636   $ N
      8016  -0.231475   $ O
      18040 -0.012838 $ Ar-40 at 99.6035 percent of natural Ar
      18036 -0.000043 $ Ar-36 at 0.3336 percent of natural Ar
      18038 -0.000008 $ Ar-38 at 0.00629 percent of natural Ar
c Concrete density = 2.3
M10    NLIB=80c PLIB=04p
       1001.60c   -0.03
       8016.60c   -0.63
       14028.60c   -0.24
```

```
       20040.60c   -0.1
c TALLY SPECIFICATION
E0 0.1 198i 20
F1:N 12.2
C1 0 1
F11:N 12.1
C11 0 1
F21:N 10.8
C21 0 1
F31:N 22
C31 0 1
F101:P 12.2
C101 0 1
F111:P 12.1
C111 0 1
F121:P 10.2
C121 0 1
F131:P 22
C131 0 1
FILES 21 DAF_2inlead
DBCN
PRDMP 2J 1
```